GEOPHYSICS®

Distributed acoustic sensing of ocean-bottom seismo-acoustics and distant storms: A case study from Svalbard, Norway

Journal:	*Geophysics*
Manuscript ID	GEO-2022-0435.R2
Manuscript Type:	Case Histories
Keywords:	DAS (distributed acoustic sensors), oceanography, passive seismic, marine, near surface
Manuscript Focus Area:	Case Histories, Passive Seismic and Microseismic Methods

Distributed acoustic sensing of ocean-bottom seismo-acoustics and distant storms: A case study from Svalbard, Norway

Kittinat Taweesintananon[*,†,‡,††], **Martin Landrø**[*,†], **John Robert Potter**[*,†], **Ståle Emil Johansen**[†,§], **Robin André Rørstadbotnen**[*,†], **Léa Bouffaut**[*,**], **Hannah Joy Kriesell**[*], **Jan Kristoffer Brenne**[†,¶], **Aksel Haukanes**[¶], **Olaf Schjelderup**[‖] and **Frode Storvik**[‖]

[*] *Acoustics Group, Department of Electronic Systems, Norwegian University of Science and Technology (NTNU), Trondheim 7491, Norway.*

[†] *Centre for Geophysical Forecasting, Norwegian University of Science and Technology (NTNU), Trondheim 7491, Norway.*

[‡] *PTT Exploration and Production Public Company Limited (PTTEP), Bangkok 10900, Thailand.*

[§] *Department of Geoscience and Petroleum, Norwegian University of Science and Technology (NTNU), Trondheim 7031, Norway.*

[¶] *Alcatel Submarine Networks Norway AS, Tiller 7075, Norway.*

[‖] *Uninett AS, Trondheim 7030, Norway.(From 2022-01-01, Uninett AS is a part of Sikt, Trondheim 7030, Norway.)*

[**] *Léa Bouffaut is now at K. Lisa Yang Center for Conservation Bioacoustics, Cornell Lab of Ornithology, Cornell University, Ithaca, NY 14850, USA.*

[††] *Corresponding author: Kittinat Taweesintananon*

(kittinat.taweesintananon@ntnu.no)

(January 31, 2023)

GEO-2022-0435.R2

Running head: **DAS of seismo-acoustics and storms**

ABSTRACT

Distributed acoustic sensing (DAS) leverages an ocean-bottom telecommunication fiber-optic cable into a densely sampled array of strain sensors. We demonstrate DAS applications to passive acoustic monitoring (PAM) through an experiment on a submarine fiber-optic cable in Longyearbyen, Svalbard, Norway. We show that DAS can measure many types of signals in the frequency range from 0.01 to 20 Hz generated by dynamics in the atmosphere, ocean, and solid earth. These include ocean-bottom loading pressure fluctuation of ocean surface waves generated by storms, winds and airflow turbulence, shear-wave resonances in low-velocity near-surface sediments, acoustic resonances in the water column, and propagating seismic waves. We show that DAS can record high-quality, low-frequency seismo-acoustic waves down to 0.01 Hz, which could be used for subsurface exploration. Using the shear-wave resonances recorded by DAS, we can determine the subsurface structure of near-surface sediments with low velocity. In addition, we can trace ocean swells back to their origins of distant storms as far as 13,000 km away from the cable. Because DAS is capable of seismo-acoustic monitoring with high spatial resolution of $\sim$ 1 m over the cable of $\sim$ 100 km long and with a broadband sensitivity down to 0.01 Hz on

the low end, it can deliver great scientific value to ocean observation and geophysics community.

INTRODUCTION

The Earth's atmosphere and oceans are continuously in coupled motion. These complex motions and interactions determine both weather and, over the longer term, the climate of the planet. Oceans play a significant role in climate, because they can retain heat and distribute it around the globe (Schmitt, 2018). Large-scale ocean currents, which are driven by variations in water density caused by temperature and salinity gradients, influence the climate by exchanging heat and water with the atmosphere. A change in ocean dynamics could induce major climate variations over large areas of the Earth in the long term (Bigg and Hanna, 2016). Hence, ocean surface winds, currents, and surface gravity waves are key climate variables that induce exchanges of momentum, energy, heat, salinity, gases, and other tracers between the ocean and atmosphere (Villas Bôas et al., 2019).

Ocean surface gravity waves (OSGWs) have random properties and evolve from complex mechanisms, where gravity is the principal restoring force. Their modern studies started in the 1940s (Mitsuyasu, 2002; Wunsch, 2021), with seminal contributions from Sverdrup (1947), Stommel (1948) and Munk (1950). Wind blowing on a water surface generates OSGWs, which are modulated via breaking and nonlinear interactions. The wave breaking affects exchanges between sea and atmosphere (Cavaleri et al., 2012). Therefore, OSGWs are an important factor in the air-sea momentum transfer. Moreover, OSGWs are a primary source of turbulence in the upper ocean, so that they directly affect navigation, offshore structure design, and coastal erosion (Abolfazli et al., 2020). However, they are not used explicitly in constraining most ocean-atmosphere models, because high-spatial-resolution (spatial sampling under 25 km) two-dimensional (2D) measurements of waves are normally unavailable. Such measurements could significantly improve ocean models (Wu et al., 2019).

Many instruments have been developed to measure directional OSGWs (European cooperation in science and technology Action 714, Working Group 3, 2005). The classical methods such as spatial arrays and pitch-and-roll buoys have been complemented by new technologies such as displacement and Global Positioning System (GPS) buoys, acoustic Doppler current meters, microwave and marine radars, coastal high-frequency radars, and real and synthetic aperture radars. However, none of these instruments can provide all the data needed to make a complete and robust estimate of the directional properties of OSGWs. Data with high spatial resolution and extensive spatial coverage would be necessary to overcome this limit. In principle, subsurface instruments that measure ocean-bottom pressure fluctuations due to OSGWs could be deployed in spatially extended arrays for accurate estimation of swell directional spectra, but this would be prohibitively expensive. Therefore, compact subsurface instruments, of which the dimensions are smaller than the typical wavelength, are more widely used by the oceanographic community. Ardhuin et al. (2019) review the modern measurement techniques of OSGWs and discuss key requirements for future sea state observation.

Distributed acoustic sensing (DAS) is a technology that can exploit the optical fiber in standard telecommunication cables as an extended spatial array of acoustic sensors (Hartog, 2017). Over 1.3 million kilometers of submarine telecommunication cables have been deployed around the Earth. Many optical fibers in these cables, often 'spares', are not currently used for telecommunication. It is possible to repurpose these unused 'dark' fibers to serve as ocean-bottom distributed acoustic sensors to measure, among other signals, dynamic strains caused by ocean-bottom pressure fluctuations. DAS measures the strain fluctuations at each sensing element of an optical fiber. A DAS interrogator can measure the strain data along the fiber with a length up to 171 km in a controlled experiment (Waagaard et al., 2021). Therefore, DAS can form spatially extended arrays with very large dimension compared to the typical length of OSGWs. In addition, DAS measures data with a spatial sampling interval of as little as 1 m, which creates arrays of many tens of thousands of sensors at relatively low cost.

DAS in submarine fiber-optic cables can measure pressure fluctuations at the ocean bottom, originating from a variety of sources (Landrø et al., 2022). DAS in ocean-bottom telecommunication fiber-optic cables can detect ocean surface gravity waves, microseisms and earthquakes (Lindsey et al., 2019; Sladen et al., 2019). Furthermore, Williams et al. (2019) demonstrate that DAS can record the seismic waves from a distant earthquake, OSGWs, and Scholte waves. However, their spectral analyses were performed on a data record of only one-hour. DAS data with a longer recording length are necessary for studying the dynamics of ocean swells, which are OSGWs originating from distant storms. For example, Zhan et al. (2021) show several dispersed signals from ocean swells from distant storms in a spectrogram computed over 11 days of the fiber-optic sensing data using the state of polarization technique.

In this article, we show that DAS can be used as a valuable tool for studying ocean dynamics. First, we describe the DAS data used in our study and their acquisition parameters. Second, we review the mechanisms of the ocean-bottom vibrations that are recorded by DAS along an ocean-bottom telecommunication cable. We also review the characteristics of the DAS data corresponding to different mechanisms of the ocean-bottom vibrations. Then, we discuss the results of our analysis related to OSGWs corresponding to distant storms. Finally, we address some potential applications of DAS in the oceanographic and geophysics communities.

METHODS

Data acquisition

We used a standard single-mode G.652D fiber within an existing submarine telecommunication cable, which was installed into soft sediments at 0–2 m below the seafloor, from Longyearbyen to Ny-Ålesund in Svalbard, Norway (Figure 1). The cable is about 250 km long and contains 24 fibers. Here we used one available dark fiber for DAS recordings, reaching about one half of the total cable length. The cable is owned and operated by Uninett AS (merged into Sikt in January 2022), which is the National Research and Education Network (NREN) in Norway.

We connected an OptoDAS interrogator, developed by Alcatel Submarine Networks, to the cable end onshore Longyearbyen. The OptoDAS interrogator sends linear optical frequency-modulated swept pulses into the fiber and receives backscattered pulses from inhomogeneities in the fiber (Waagaard et al., 2021). It calculates the time-differentiated phase changes of consecutive backscattered pulses corresponding to every spatially sampled position along the fiber. These are used to estimate the longitudinal strains of the fiber at each sampling point.

In this experiment, we use light pulses with a free-space wavelength of 1,550 nm and a sampling period of 1×10^{-8} s at the optical receiver. Defined by regions of interest, we extract 30,000 channels sampled every 4.08 m along the fiber from 0 to 120 km from the interrogator. Figure 1 shows a map of the active DAS array used in our experiment. DAS data were continuously recorded using 1.55 ms time sampling interval throughout the survey. The gauge length is 8.16 m. The backscattered signal strength decays by ≈ 0.2 dB/km along the cable, amounting to -40 dB over 100 km. We acquired data over 44 days from 2020-06-23 to 2020-08-05, and transferred them in near-real-time to NTNU in Trondheim over Uninett's telecommunication network for further analysis.

Data processing

The phenomena investigated in this study occur below 20 Hz. Therefore, we resample the DAS strain data from 1.55 to 20 ms with an antialiasing filter at 80% of the output Nyquist frequency. The resampled data with the Nyquist frequency of 25 Hz are used in our analysis. Data resampling also reduces the computational cost for analyzing data over a long time window. We also attenuate interrogator noise that occurs in the whole DAS array, where the noise model is obtained by stacking all the DAS data traces from onshore channels in a calm environment. To understand the characteristics of the data corresponding to different mechanisms of the ocean-bottom vibrations, we compare the processed data with and without the excitation from seismic waves. With this comparison, we can distinguish seismo-acoustic signals from ocean-bottom pressure fluctuation exerted by loading under ocean surface waves.

To distinguish different wave types, we analyze DAS strain data in different domains including the time-distance (t-x) domain, the frequency-distance (f-x) domain, the time-frequency (t-f) domain (also called 'spectrogram'), the frequency-wavenumber (f-k) domain, and the frequency-velocity (f-v) domain.

Mechanisms of ocean-bottom vibrations

The strain of a fiber section is a function of its particle motion along the fiber (Lior et al., 2021). Based on Newton's second law of motion, the particle acceleration along the fiber can be induced by the force endowed with the pressure changes with distance (i.e., a pressure gradient) along the fiber (Stull, 2017, Ch. 10). Based on Hooke's law in elastic media, the strain of the fiber section is proportional to that component of the pressure gradient projected along the direction of the fiber (Robein, 2010, Ch. 1). The transfer function between seafloor displacements and pressure fields associated with OSGWs, which is called the seafloor compliance, is discussed in Crawford et al. (1991). Therefore, pressure changes in space and time are detectable by DAS at the seafloor, providing they cause strains above the detection limit (due to noise) in the order of 1 nε (nano-strain unit).

Ocean-bottom vibrations are excited by two mechanisms. The first mechanism is the loading pressure change under an overlying wave, which is attributed to atmosphere and ocean dynamics. The second mechanism is an interaction of the ocean-bottom and the propagating seismo-acoustic waves, which are generated by an earthquake, explosion, or similar energetic source. In this context, seismo-acoustic waves include not only compressional (P-) waves, but also shear (S-) waves and interface waves.

Loading pressure responses

The total or absolute pressure under an overlying wave like OSGWs is the summation of dynamic and static pressures. The dynamic component is the pressure fluctuation caused by the wave motion. In contrast, the static component comprises the atmospheric pressure and the hydrostatic pressure corresponding to the weight of the overlying water body.

For a progressive wave with small amplitude, we consider an OSGW as a simple sinusoidal wave profile as a function of time t and the x and y coordinates on the horizontal plane:

$$\eta\left(x,y,t\right)=a\cos\left(k_x x+k_y y-\omega t\right)\ , \tag{1}$$

where η is the elevation of the water surface relative to the still-water level (SWL), a is the wave amplitude equal to one half of the wave height (the vertical distance to its crest from the preceding trough), $\omega=2\pi f$ is the angular frequency, and k_x and k_y are the x- and y-components of the horizontal angular wavenumber $k=$

$2\pi/\lambda = \sqrt{k_x^2 + k_y^2}$. Here, f and λ are the frequency and wavelength of the OSGW, respectively. Hence, the total pressure at the vertical displacement z from SWL is given by (Coastal Engineering Research Center, 1984)

$$P_{\text{total}}(x, y, t, z) = \rho g \frac{\cosh(k(z+H))}{\cosh(kH)} \eta(x, y, t) - \rho g z + P_a\,, \tag{2}$$

where z equals zero at SWL and is negative downward (toward the seafloor), H is the water depth (the depth measured from SWL to the seafloor), ρ is the mass density of water, $g \approx 9.81$ m/s^2 is the gravitational acceleration, and P_a is the atmospheric pressure. On the right-hand side of equation 2, the first term represents a dynamic component, whereas the second and the third terms are the hydrostatic and atmospheric pressures, respectively.

Because only the dynamic component is transferred to strains measured by ocean-bottom DAS, we derive the dynamic pressure at the seafloor ($z = -H$) from equation 2 as

$$P_{d,\text{osgw}}(x, y, t, z = -H) = P_{\text{total}} - \rho g H - P_a = \frac{\rho g \eta(x, y, t)}{\cosh(kH)}\,. \tag{3}$$

Because this dynamic loading pressure is a direct impact of the OSGW $\eta(x, y, t)$ as shown in equation 1, it has the same dispersion relation as the OSGW (Airy, 1841; Craik, 2004):

$$\omega^2 = gk \tanh(kH)\ . \tag{4}$$

In addition, equation 3 implies that the dynamic loading pressure at the seafloor decays exponentially with water depth through the hyperbolic cosine function.

We may define the maximum frequency limit of OSGWs as the highest frequency at which OSGW dynamic loading pressure is observable using the same approach as Williams et al. (2022) based on Crawford et al. (1991). Let $n = \lambda/H$ be the ratio between wavelength to water depth, so that the angular wavenumber can be written as $k = 2\pi/(nH)$, and, hence, the frequency of OSGWs is derived from equation 4 as

$$f_{\mathrm{osgw}} = \sqrt{\frac{g}{2\pi n H} \tanh\left(\frac{2\pi}{n}\right)}. \tag{5}$$

By using $n = 0.827$ with an approximation that $\tanh(2\pi/n) \approx 1$, we derive the maximum frequency of OSGWs from equation 5 as

$$f_{\mathrm{osgw,max}} \approx \sqrt{\frac{g}{2\pi H \times 0.827}}. \tag{6}$$

This maximum frequency corresponds to the dynamic loading pressure with sufficiently low magnitude at $P_{d,\mathrm{osgw}} \approx 0.001 \times \rho g \eta$. Here, we derive equation 6 by using $n = 0.827$ in equation 5, such that the corresponding dynamic loading pressure (using $1/\cosh(kH) = 1/\cosh(2\pi/n) \approx 0.001$ in equation 3) has sufficiently low magnitude at 0.1% of the dynamic loading pressure at SWL, i.e., $P_{d,\mathrm{osgw}} \approx 0.001 \times \rho g \eta$. This low magnitude threshold is lower than the threshold of 0.37% using $n = 1$ in Williams et al. (2022). Note that the choice of selecting this low magnitude threshold is arbitrary. It can be any sufficiently low number that highlights the high frequency limit of observable OSGWs in DAS data.

Tide can also affect OSGW dynamic loading pressure at the seafloor as discussed in Williams et al. (2022). Here we derive an explicit formula of its maximum frequency in the presence of tide, which causes SWL to change with time. Let $\zeta(t)$ be the sea-level change defined as the vertical displacement with positive upward from the mean-sea level (MSL) to the time-variant SWL. Then, the water depth is written as $H(t) = H_{\text{avg}} + \zeta(t)$, where H_{avg} is the time-invariant depth measured from MSL to the seafloor. From equation 2, we derive the dynamic pressure at the seafloor associated with OSGWs and tide as

$$P_{d,\text{osgw-tide}}\left(x,y,t,z=-H\right) = P_{\text{total}} - \rho g H_{\text{avg}} - P_a = \frac{\rho g \eta\left(x,y,t\right)}{\cosh\left(k\left(H_{\text{avg}}+\zeta(t)\right)\right)} + \rho g \zeta(t)\,. \tag{7}$$

From equation 4 based on equation 7, we can determine the maximum frequency of OSGWs corresponding to the sufficiently low dynamic pressure at $P_{d,\text{osgw-tide}} \approx 0.001 \times \rho g \eta$:

$$f_{\text{osgw-tide,max}} = \frac{1}{2\pi}\sqrt{g k_{\text{osgw-tide,max}} \tanh\left(k_{\text{osgw-tide,max}}\left(H_{\text{avg}}+\zeta(t)\right)\right)}\,, \tag{8}$$

where

$$k_{\text{osgw-tide,max}} = \frac{1}{H_{\text{avg}}+\zeta(t)}\,\text{arccosh}\left(\frac{\eta}{0.001\times\eta-\zeta(t)}\right)\,. \tag{9}$$

Equation 9 only exists if $0 \le 0.001 \times \eta - \zeta(t) \le \eta$. Later in this article, we visualize the effect of tide on the maximum frequency of OSGW dynamic loading pressure at the seafloor by simply applying $\eta = 1000 \times \zeta_{\text{max}}$ to equations 8 and 9. Here ζ_{max} is the maximum sea-level change from MSL over the entire recording period.

It is important to note that any ocean surface wave can cause dynamic loading pressure on the seafloor. The ocean surface waves can be classified by wave period or frequency, disturbing force, and restoring force (Coastal Engineering Research Center, 1984). For the waves in the frequency range from 0.01 to 20 Hz, ocean surface waves are typically generated by friction exerted by winds on the ocean surface. Either gravity or surface tension can be the principal restoring force, i.e., the force that attempts to return the fluid to its equilibrium position. OSGWs have gravity as the restoring force. They are called 'seas' when the waves are under the influence of local wind in a generating area, and they are called swells when the waves move out of the generating area and are no longer influenced by significant wind action. On the other hand, the ocean surface waves are called capillary waves, when the surface tension is the principal restoring force. The ocean surface waves that are affected by both gravity and surface tension are called gravity-capillary waves (Părău et al., 2005). The impact of surface tension on the wave amplitude is lower than gravity, such that the dynamic loading pressure on the seafloor is dominated by OSGWs.

Nevertheless, strong winds and airflow turbulence may cause unstable ocean surface waves and disruptions to the sea surface. Surface disruptions like wave breaking could cause additional forces and, hence, slamming pressure onto the ocean bottom. Breaking wave loads are an element of dynamic loading pressure on the seafloor. Reviews of breaking waves and their characteristics in deep and intermediate waters can be found in, e.g., Perlin et al. (2013), Robertson et al. (2013), and Barthelemy et al. (2018). In addition, the slamming pressure resulting from breaking wave loads in shallow water is studied by Yang and Cai (2022). However, the wave-breaking mechanism and the breaking wave loads onto the seafloor, especially in deep and intermediate waters, have not been fully understood and are still under research.

Seismo-acoustic responses

Seismo-acoustic waves propagating through the seawater and the solid earth cause strain fluctuation in an ocean-bottom fiber-optic cable upon their arrivals. Seismo-acoustic waves are emitted by a great variety of sources from both natural and anthropogenic origins, as discussed in Schwardt et al. (2022). At some specific frequencies equal or close to the natural frequencies (also known as eigenfrequencies) of the system, the seismo-acoustic waves can excite modes of vibration in the media where they are propagating, which are called standing waves or normal modes. Normal modes can occur naturally in any layer and be caused by either P- or S-waves, even in the absence of any external driving force. In each mode, the wave amplitude significantly increases if we apply a periodic force with the frequency close to the natural frequency. This phenomenon is called resonance.

In the seawater, seismo-acoustic waves can propagate in a long range via bottom-interacting paths in the form of guided waves at different propagation modes (Landrø and Hatchell, 2012). The lowest frequency in which a certain mode can propagate is the cutoff frequency. That is, a cutoff frequency is the critical frequency below which the water channel ceases to act as a waveguide, causing energy radiated by the source to propagate directly into the bottom (Jensen et al., 2011). The cutoff frequencies for the guided waves in the water layer can be determined from

$$f_n = \frac{(2n-1)\,c_w}{4H\sqrt{1-(c_w/c_p)^2}}\,, \tag{10}$$

where n is a positive integer, indicating the order of the normal mode (Landrø and

Hatchell, 2012). This expression is exact only for a homogeneous water column with water depth H and sound speed c_w overlying a homogeneous bottom with sound speed c_p. In the case of rigid seafloor ($c_w/c_p \ll 1$), the cutoff frequencies in equation 10 can be written as

$$f_n \approx \frac{(2n-1)\,c_w}{4H}\,. \tag{11}$$

Assuming that the P-wave velocity in the seafloor is higher than the P-wave velocity in the water, we use equation 11 as a simple guide in this article to characterize the normal modes of acoustics in the water layer.

At a soft sedimentary seafloor (a fluid-solid interface), of which the S-wave velocity in the bottom layer (c_s) is much lower than the P-wave velocities in the water (c_w) and the bottom layer (c_p), there exists the Scholte interface mode (the zeroth mode). This Scholte interface mode has no cutoff frequency, and its (horizontal) phase velocity is identical with the Rayleigh-wave velocity for extremely low frequencies and approaches the Scholte-wave velocity for extremely high frequencies (Rauch, 1980). Rising the frequency scale, the dispersion curves for (horizontal) phase velocities of the higher-order modes correspond to the propagation modes of the body waves (either P- or S-waves) in both layers above and below the fluid-solid interface, i.e., the water and ocean-bottom layers (Westwood et al., 1996).

Wave propagation modes can occur for either P- or S-waves in any solid layer below the seafloor. S-wave resonances can be observed at frequencies between 0.3 and 7.5 Hz, when surficial marine sediments over a rock substrate have low S-wave velocities (Godin et al., 2021). These resonances are generated by normal reflection of

S-waves. The S-wave resonance as well as the normal modes and propagation modes of S-waves in the seafloor sediments are discussed and studied in several publications (Webb, 1998; Stephen et al., 2003). Based on the theoretical explanation given by Godin and Chapman (1999), we may investigate this phenomenon using a power-law S-wave velocity profile of the soft seafloor sediments in the form $c_s\left(z_s\right) = c_{s,0} z_s^{\nu}$, where z_s is the depth below the seafloor (a fluid-solid interface). Here, $c_{s,0}$ and ν are the two non-negative constants, whereas z_s equals zero at the seafloor and is positive downward (toward the center of the Earth). Let $z_s = H_s$ be a rigid boundary, so that the soft-sediment thickness is equal to H_s. According to Godin and Chapman (1999, Eq. 17), the n-th S-wave resonance frequency can be determined from

$$f_{s,n} = \frac{c_{s,0}\left(1-\nu\right) j_{m,n}}{2\pi H_s^{1-\nu}}\,, \tag{12}$$

where n is a positive integer indicating the order of the normal mode, $m = \frac{2\nu-1}{2(1-\nu)}$ is a monotonically increasing function of ν, and $j_{m,n}$ is the n-th positive zero of the Bessel function $J_m(x)$. For $n \gg 1 + m^2$, we can apply the asymptotic expansion for the Bessel function zeros to equation 12, then we obtain (Godin and Chapman, 1999, Eq. 18)

$$f_{s,n} \approx \frac{\left(n + \frac{m}{2} - \frac{1}{4}\right) c_{s,0}\left(1-\nu\right)}{2H_s^{1-\nu}} + \mathcal{O}\left(\frac{1}{n}\right)\,. \tag{13}$$

For the homogeneous sediment with a constant S-wave velocity ($\nu = 0$ giving $c_s = c_{s,0}$ and $m = -\frac{1}{2}$), equation 13 has the same form as the cutoff frequencies in the homogeneous water layer in equation 11, i.e., $f_{s,n} \approx \left(2n-1\right) c_{s,0} / \left(4H_s\right)$.

Later in this article, we show that ocean-bottom DAS can measure the S-wave modes in seafloor sediments. Using the relation in equation 13, we can determine the seafloor soft-sediment thickness (H_s) from the first S-wave resonance frequency ($f_{s,1}$), which is estimated from the frequency analysis.

Origin of ocean swells

Ocean-bottom seismic sensors can detect the loading pressure associated with ocean swells generated from large storms occurring several thousand kilometers away. Bromirski and Duennebier (2002) discuss the amplitude characteristics and wave spectra of these swells. The dispersion relation for OSGWs in deep water predicts that low-frequency waves will arrive before higher-frequency waves. Also, it depicts the resulting linear up-sweep characteristics of ocean swells in spectrograms (time-frequency representations) computed from ocean-bottom seismic data (Bromirski and Duennebier, 2002, fig. 11). Using the method described in Lin et al. (2018) based on Munk et al. (1963), we can also trace ocean swells, measured by DAS, back to their originating distant storms. We use the time-frequency gradients measured in spectrograms to calculate the great-circle distances and traveltimes of the storm-induced ocean swells traveling from the storm centers to the DAS receiver.

Lin et al. (2018), based on Munk et al. (1963), derive the expression for the propagation distance of an ocean swell as

$$x = \frac{g}{4\pi\left(\frac{df}{dt}\right)}, \tag{14}$$

where f is the frequency of the ocean swell. Here, df/dt is the time-frequency gradient or slope of the linear up-sweep trend. Further, the group velocity (c_g) of the swell in deep water can be computed from

$$c_g = \frac{1}{2}\sqrt{\frac{g}{k}} \approx \frac{g}{4\pi f}, \tag{15}$$

where f is the frequency of the wave. We can, then, estimate the traveltime (t) of the ocean swell from the storm center to the DAS receiver from

$$t = \frac{x}{c_g}. \tag{16}$$

In short, we first estimate the slope of a linear up-sweep trend in the spectrogram and determine the propagation distance of the swell using equation 14. Next, we use the start frequency of the trend in the spectrogram to compute the group velocity and the traveltime using equations 15 and 16, respectively. The estimated distance and traveltime help to characterize the storms that produced the observed ocean swells.

RESULTS AND DISCUSSION

Data characterization

Based on our analysis of the data in the frequency range between 0.01 and 20 Hz, we observe six signatures associated with different wave types in the ocean-bottom DAS strain data in Svalbard. Figures 2–8 are used to identify the phenomena behind the six wave types marked as Events 1–6 in Figure 3. These phenomena shall be discussed in details in the next subsections, but we here provide a brief overview as follows. Events 1–3 are associated with the loading pressure responses of ocean swells (OSGWs originating from distant storms), OSGWs exerted by winds, and ocean surface disruptions caused by strong winds and airflow turbulence, respectively. In contrast, Events 4–6 belong to the following seismo-acoustic responses, respectively: S-wave resonances in the seafloor sediments, seismic waves generated from various sources (earthquakes, microseisms, anthropogenic sources, etc.), and acoustic propagation modes in the water channel.

This section is structured into three subsections. First, we introduce the data and relevant illustrations used for characterizing different wave types in ocean-bottom DAS data. Second, we discuss the wave phenomena related to the ocean-bottom loading pressure responses. Last, we discuss the seismo-acoustic responses observed in the ocean-bottom DAS data.

Data description

On 2020-07-22 at 06:12:44 (UTC), an earthquake with a moment W-phase magnitude (M_{ww}) of 7.8 occurred at a depth of 28 km approximately 100 km south of the Alaska Peninsula (Figure 1A). The earthquake was detected by seismic stations worldwide and our DAS array near Longyearbyen, which is approximately 5,100 km away from the epicenter on a great circle. At the DAS channel at 36 km inline distance from the shore, the approximate arrival times of the P-, S- and SS-waves are at 510, 950 and 1,200 s, respectively, from the earthquake's origin time.

We compare the DAS strain data before and after the seismic waves from the earthquake in Alaska arrive. As shown in Figure 2A, the data in the 1,200-s time window from 2020-07-22T06:00:02Z contain no seismic waves from significant earthquakes. In contrast, Figure 2B shows the data in the 1,200-s time window from 2020-07-22T06:20:02Z that contain strong seismic waves from the earthquake in Alaska. The P-, S- and SS-waves arrive to the DAS array at 72, 512 and 762 s from 2020-07-22T06:20:02Z, respectively. The seismic waves are marked as Event 5 in the figure (for consistency with the annotation in Figure 3). In this article, our discussion is made mostly based on a series of figures representing different domains of the data from the two 1,200-s time windows shown in Figure 2.

From Figure 2A, we observe low-frequency right- and left-dipping wavetrains (marked as Event 1) with the apparent velocity about 30 m/s in all the channels from 0 to 15 km from the shore, where the water depth ranges from 0 to 280 m. In addition, we observe right- and left-dipping wavetrains (marked as Event 2) with the higher frequency and the lower apparent velocity at 20 m/s only in the shallow water with less than 100 m water depth.

Figures 3A&B show the f-x spectral analysis from 0.01 to 20 Hz of processed DAS strain data from the 1,200-s time window before the arrivals of strong seismic waves from the Alaska earthquake, which corresponds to the strain data in Figure 2A. Note that the processed data have a time sampling interval of 20 ms, i.e., the Nyquist frequency is 25 Hz. A power spectrum is computed by a discrete Fourier transform along the time axis of the processed data within the whole 1200-s time window, in which the normalization factor is 1 (unscaled) for the forward transform. The average power spectra over 251 channels (500 m radius) around three selected locations are shown in Figure 3A. The locations are selected to represent the data recorded at different water depths and distances from the shore. The power spectra of individual channels are combined to produce the distance-frequency plot in Figure 3B. Similarly, the f-x spectral analysis of the DAS strain data in Figure 2B, from the 1,200-s time window containing strong seismic waves from the Alaska earthquake, is shown in Figures 3C&D.

In three different frequency bands, Figure 4 shows the band-limited DAS strain data in the time window between 100 and 130 ms from 2020-07-22T06:00:02Z, i.e., the data without strong earthquake signals in Figure 2A. The band-limited data are used to understand the t-x characteristics of the wave types in different frequency bands. Based on the annotations in Figure 3A, Events 1 and 2 are observed in 0.005–0.2 Hz (Figure 4C), Events 3 and 5 are observed in 0.2–1.2 Hz (Figure 4B), and Event 4 is observed in 1.2–20 Hz (Figure 4A).

Figure 5 shows the frequency analysis on the data without strong earthquake signals from 0 to 76 km distances along the cable at the same time window as in Figure 2A. To avoid poor quality due to image downsampling, we only plot the data along 76 km distance of the fiber-optic cable in this article. Figure 6 shows the f-k spectra of the DAS strain data at four individual spatial locations, with and without strong seismic waves from the Alaska earthquake. Figure 7 shows the spectrograms of DAS strain data calculated at three individual recording channels. Figure 8 shows the same frequency analysis as Figure 5 on the data with strong earthquake signals from Alaska at the same time window as in Figure 2B.

Loading pressure responses

The 0.06-Hz peak marked as Event 1 in Figure 3B presents in all the recording channels from 0 to 15 km along the cable, where the water depth ranges from 0 to 280 m. In Figure 2A and Figure 4C, the waves associated with Event 1 are seen to propagate at the apparent velocity 30 m/s mainly toward the shore, and their reflections at the shore cause weaker wavetrains propagating back to the open ocean. As seen in Figure 3B, the frequency of Event 1 is lower than the maximum frequency of OSGWs ($f_{\mathrm{osgw,max}}$) calculated from equation 6 using the water depths from local bathymetry along the fiber-optic cable. This frequency characteristic is also observed in Figure 5B showing the frequency analysis on the data without strong earthquake signals from 0 to 76 km distances along the cable at the same time window as in Figure 2A.

If Event 1 is the dynamic loading pressure response of OSGWs, its amplitude must decay with water depth as described in equation 3. To clarify this, we will compare the root-mean-square (RMS) of amplitude at the frequency around 0.06 Hz from the f-x power spectra with an amplitude trend modeled by equation 3 as plotted in Figure 5C. In Figure 5C, we model the strain amplitude associated with OSGWs at the constant frequency 0.06 Hz using the similar approach to Williams et al. (2019, Fig. 6) as described below. First, we solve the dispersion relation in equation 4 for the angular wavenumber (k) using the Newton-Raphson method (You, 2008, Eq. 2&3). Then, we compute the dynamic pressure at the seafloor ($P_{d,\mathrm{osgw}}$) using equation 3. Finally, we convert the seafloor pressure into fiber strain by multiplying $P_{d,\mathrm{osgw}}$ with a scaling factor, which is determined by data fitting for a linear relationship between pressure and strain. This model assumes that OSGW amplitude (one half of the wave height) is invariant with water depth.

Figure 5C compares the powers corresponding to the observed RMS amplitude and the modeled amplitude at 0.06 Hz. We observe a good correspondence between the observed and modeled amplitude for the distance greater than 20 km from the shore. In contrast, the strain amplitude of Event 1 in the inner part of the Isfjord (< 20 km from the shore) is obviously weaker than the modeled amplitude. This amplitude mismatch implies that the OSGW amplitude in the inner part of the Isfjord is smaller than the wave in the deeper water in the outer part. According to Kakinuma and Kusuhara (2022), the amplitudes of ocean-surface waves depend on not only the water depth but also the width of the water channel (lateral). Because the width of the Isfjord mostly increases from the outer to the inner parts (from West to East), the OSGW amplitude in the inner part near Longyearbyen tends to be lower than the OSGW amplitude in the outer part. Hence, the amplitude mismatch of Event 1 and the OSGW model in Figure 5C could be an effect of the topography of the water channel.

Figure 6 shows the f-k spectra of the DAS strain data at four individual spatial locations, with and without strong seismic waves from the Alaska earthquake. In all the f-k spectra, we observe that the 0.06-Hz peak is aligned with the OSGW dispersion curve (blue dashed line) which is calculated from equation 4. From the spectrograms in Figure 7, we observe that the frequency of Event 1 slowly increases with time.

According to equation 14, the low time-frequency gradient or slope of Event 1 implies that the sources of OSGWs are thousands of kilometers away from Svalbard. Thus, Event 1 corresponds to the loading pressure fluctuation associated with the overlying ocean swells originating from distant storms. In the next subsection, we study Event 1 for storm monitoring in more details.

The 0.12-Hz peak marked as Event 2 in Figure 3B is pronounced only in shallow water (< 100 m deep) within 5 km distance from the shore. The water depth profile is shown in Figure 2C. In Figure 2A and Figure 4C, the waves associated with Event 2 are observed clearly in the 5 km distance from the shore. They propagate approximately at the apparent velocity 20 m/s toward with reflections backward the shore. As seen in Figure 3B, the frequency of Event 2 is higher than Event 1 but lower than the maximum frequency of OSGWs ($f_{\mathrm{osgw,max}}$) calculated from equation 6. The amplitude of Event 2 is bound by this maximum frequency limit in all recording channels along the cable, as shown in Figure 5. By conforming to this frequency limit, the amplitude of Event 2 decays with water depth exponentially, as described in equation 3. In Figure 6, we observe in the f-k domain that Event 2 is generally aligned with the OSGW dispersion curve (blue dashed line) calculated from equation 4. The small deviation of Event 2 from the OSGW dispersion curve occurs when the propagating direction of an OSGW is oblique to the cable axis. Therefore, we conclude that Event 2 is the dynamic loading pressure response of OSGWs excited by winds.

Because Events 1 and 2 are direct responses to OSGWs, their amplitude and frequency must be affected by tide described in equations 7 and 8, respectively. Figure 7 shows the spectrograms for three individual channels along with tide and weather data in the study area. The maximum frequency limit of OSGWs ($f_{\text{osgw-tide,max}}$) from equation 8 is plotted in red. Here, we can observe that the high-frequency OSGWs, i.e., Event 2, are strongly modulated by sea-level changes caused by tide. The variation of amplitude and frequency in shallow water (Figure 7A) is larger than deep water (Figure 7C). In Figure 7A, we clearly see that both the spectral amplitude and the maximum frequency of OSGWs become highest at high tide (high sea level) plotted in Figure 7D. This tidal modulation of OSGWs agrees with their maximum frequency limit defined in equation 8, which indirectly validates the dynamic pressure response in equation 7. Note that our observation here is different from Williams et al. (2022, Fig. 3), in which they infer that the spectral amplitude and the maximum frequency become highest during low tide with frequency-dependent phase delays affected by non-linear wave-current interaction. We believe that their observation could be explained by equation 8 in this article.

The energy peak at 1.0–1.2 Hz is marked as Event 3 in Figures 3 and 5. Like Event 2, Event 3 can be observed only in shallow water ($<$ 100 m deep) within 5 km distance from the shore. This implies that the amplitude of Event 3 decays with water depth in a similar fashion to Event 2. However, we see that the frequency of Event 3 is almost invariant with water depth. Because the frequency of Event 3 is not a function of water depth, Event 3 does not involve seismo-acoustic wave propagation in the water layer. In addition, because its amplitude decays with water depth to a greater extent than spherical divergence, Event 3 does not involve seismo-acoustic wave propagation from earthquakes or other seismic sources. Hence, Event 3 may result from dynamic loading pressure on the seafloor caused by some wave motions above.

As observed in Figures 3 and 5, Event 3 has a higher frequency than the maximum frequency limit of OSGWs. Therefore, Event 3 is definitely not caused by an OSGW. In Figure 4B, we observe that the waves associated with Event 3 are scattered with unclear patterns across time and space axes. However, we can estimate from the same figure that the apparent velocity of their diffraction tails could be as high as 200 m/s. This estimation agrees with the f-k spectrum in Figure 6C. The velocity is too high for Event 3 to be interpreted as ocean surface waves or ocean currents.

One possible generating mechanism of Event 3 could be an effect of slamming pressure exerted onto the seafloor caused by turbulence in the upper ocean or ocean surface disruptions like wave breaking. Weather and wind conditions can affect the frequency of such surface disruptions and their subsequent ocean-bottom pressure. In addition, the slamming pressure on the seafloor caused by these disruptions could be impulsive and strong enough to generate seismo-acoustic waves like P-waves, S-waves and Scholte interface waves. The Scholte interface waves, which longitudinally propagate along the seafloor, can be measured by ocean-bottom DAS and have relatively high amplitude responses (Spica et al., 2022). In addition, the apparent velocity of 200 m/s for Event 3 is reasonable for the Scholte-wave velocity, which is typically on the order of 0.86 times the S-wave velocity (c_s) in the seafloor sediments if $c_s < c_w$

(Westwood et al., 1996).

Figures 7A&B show the spectrograms from two channels in shallow water. We clearly see that the frequency of Event 3 varies with time. Its amplitude is also strongest during strong wind condition (high wind speed), as compared with the wind speed data especially from the Isfjord Radio weather station in Figure 7D. Because the amplitude of Event 3 is modulated with the wind speed and its apparent velocity matches with the Scholte-wave velocity at the seafloor, we believe that Event 3 has a relation with Scholte interface waves generated from the dynamic ocean-bottom loading pressure caused by wind-driven ocean surface disruptions. More detailed studies are required to verify our speculation on Event 3.

Seismo-acoustic responses

Event 4 marked on the f-x spectra in Figures 3 and 5 is observed in all the recording channels along the cable. Its frequency is spatial-variant. Event 4 is associated with harmonic wave patterns. As in Figure 5, the first harmonic is observed in the data even in the absence of strong seismic waves from earthquakes. When strong seismic waves from the Alaska earthquake dominate the data (Figure 8A), the harmonics at the higher orders can be observed as shown in Figure 8B. Because Event 4 occurs naturally and can be enhanced by external seismic waves, we relate Event 4 to normal modes driven by seismo-acoustic waves.

In Figures 5B and 8B, the first (f_1) and second (f_2) cutoff frequencies for the guided acoustic waves in the water layer are plotted as black dashed lines on the f-x

spectra. Here, the cutoff frequencies are calculated from equation 11 using the water sound speed $c_w = 1490$ m/s and the water depth profile along the fiber-optic cable. In the f-x spectra, the energy peak associated with Event 4 does not spatially conform to these water-related cutoff frequencies, especially in the shallow water within 5 km distance from the shore. Hence, Event 4 must be associated with the normal modes in a different layer than the water layer.

The time-invariant frequency of Event 4 as shown in Figure 7 also confirms that Event 4 is not related to normal modes in the water column, of which the thickness varies with time due to tide. The f-k spectra in Figure 6 show that Event 4 is dispersed and its apparent phase velocity is between 100 and 1,000 m/s. From the figure, the apparent phase velocity approximately decreases from 1,000 to 200 m/s by increasing the frequency above the cutoff frequency for S-wave modes. Because its velocity is significantly lower than the water sound speed ($\sim$ 1,490 m/s) and subsurface P-wave velocity, Event 4 should involve S-wave propagation below the seafloor.

According to Albaric et al. (2021), we can expect the low-velocity layer (LVL) with S-wave velocity about 200 m/s in the upper 50 m of the near-surface sediments in Longyearbyen. A strong velocity contrast can be observed at about 100 m deep below the surface, in which the S-wave velocity abruptly changes from 450 to 1,800 m/s within a few meters (Albaric et al., 2021, Fig. 8). This velocity contrast may be interpreted as the interface between frozen and unfrozen strata in permafrost underlying most of the land surface in Svalbard. In Svalbard, it has low possibility to find submarine permafrost, which is the relict terrestrial permafrost that was inundated when sea levels rose after the Last Glacial Maximum (Angelopoulos et al., 2020). Therefore, we would refer the strong velocity contrast below the seafloor in Svalbard to the interface between unconsolidated sediments (the LVL) and consolidated rock strata. According to Forwick and Vorren (2011), this LVL is interpreted as the shallow glacimarine sediments below the water column in the Isfjord. Because DAS is sensitive to the particle motions along the cable axis, it is likely that Event 4 results from S-wave resonances corresponding to horizontally polarized shear (SH) wave propagation in the LVL.

We manually pick the first S-wave resonance frequency $f_{s,1}$ at the onset of the lower-frequency energy peak associated with Event 4 in the f-x spectra as plotted in Figures 5B and 8B. Based on Albaric et al. (2021), we assume the LVL to be homogeneous with the constant S-wave velocity of 200 m/s. Given the first S-wave resonance frequency $f_{s,1}$ as picked and the homogeneous S-wave velocity model, we can determine the thickness H_s of the LVL from equation 13 with $n = 1$, $\nu = 0$, $c_{s,0} = 200$ m/s and $m = -\frac{1}{2}$. As a result, we can plot the structural depths below SWL of the seafloor (H) and the LVL base ($H + H_s$) as shown in Figures 5D and 8D. As also plotted in Figures 5B and 8B, we determine the second S-wave resonance frequency $f_{s,2}$ from equation 13 using the previously estimated LVL thickness H_s.

As discussed above, we can use passive DAS recording to map the subsurface structure of the LVL below the seafloor. This also infers that we can delineate the base of shallow glacimarine sediments in the Arctic using S-wave resonance observed in DAS data. Similarly, we may use DAS to determine the structure of any other LVL such as near-surface unconsolidated sediments or weathered layers in tropical survey areas. Hence, ocean-bottom DAS is a potential tool for exploring and characterizing the near-surface geologic structure.

In this article, Event 5 denotes ocean-bottom DAS responses to seismo-acoustic waves directly propagating from any source type such as earthquakes, cryoseisms, microseisms, seismic airguns, whales, and ship propellers. Hence, we attribute Event 5 to represent seismic waves in any frequency range depending on their source types. In Figure 3A, there is a slight increase in energy around 0.36 Hz marked as Event 5 in the power spectra. An increase in energy around 0.36 Hz has been reported as the secondary microseism associated with the 0.18-Hz opposing surface gravity wave groups in an ocean-bottom DAS experiment in Belgium by Williams et al. (2019, Fig. 2). In our data, we observe no energy peak around 0.18 Hz. Moreover, the 0.36-Hz energy (Event 5) appears as flat low-frequency wavetrains in Figure 4B. This characteristic is obviously different from highly-dipping linear wavetrains associated with OSGW responses (Events 1 and 2) observed in Figure 4C. Therefore, it is unlikely that the 0.36-Hz energy directly involves OSGWs. In addition, its frequency is not close to the frequency limits of OSGWs, normal modes of acoustics in water, or S-wave resonances in the LVL below the seafloor. Thus, we believe that the 0.36-Hz energy in Figure 3A results from seismo-acoustic waves and could be marked as Event 5, although we cannot identify their seismic origins.

Figures 3C&D show the spectral analysis of DAS strain data in Figure 2B that contain strong seismic waves (P-, S- and SS-waves) from the 2020-07-22 M_{ww} 7.8 earthquake on the Alaska Peninsula. Here, the responses caused by these seismic waves arriving at the seafloor significantly boost the strain power in all the frequency below 4 Hz. This strong seismic energy is classified as Event 5, and it is superimposed on the initial ambient levels shown in Figures 3A&B. Figure 8A shows the seismic recording profile measured by DAS that contains strong seismic waves from the Alaska earthquake. The recorded data are similar to the horizontal component seismogram measured from the KBS seismic station in Ny-Ålesund. The arrival times of P-, S- and SS-waves marked in Figure 8 also agree with the KBS seismogram and the traveltimes modeled by ray tracing from the epicenter.

The particle motions perpendicular to the fiber-optic cable can be sensed by DAS with less sensitivity than the parallel motions (Taweesintananon et al., 2021). Hence, the normal modes of acoustic wave propagation in the water column marked as Event 6 are hardly observed in all the f-x spectra in Figures 3, 5 and 8. Although it is much weaker than the S-wave resonance (Event 4), we can see the energy peak for the first mode of acoustics in the water column marked as Event 6 in the f-k spectra in Figures 6A&E. Here, we observe that Event 6 is dispersed, in which its apparent phase velocity is between 1,000 and 10,000 m/s and decreases with increasing frequency above the first cutoff frequency (f_1) for acoustic normal modes in the water column.

Ocean wave monitoring

Ocean-bottom DAS can be used for monitoring low-frequency ocean-bottom vibrations corresponding to OSGWs and, hence, ocean swells. In this section, we elaborate our detailed analysis of the same DAS data for storm monitoring as presented in Landrø et al. (2022). Figure 9 shows spectrograms from three individual DAS recording channels at different water depths and distances from the shore. Figures 9A–C show the linear up-sweep trends of different ocean swells ranging from 0.04 to 0.1 Hz. Their frequencies monotonically increase with time. These linear trends correspond to the ocean swells produced by distant storms. Over the entire period of recording, we can identify 12 linear trends in the spectrograms. Most of them last between 50 and 100 hours, and can overlap in time and space.

Figure 9E shows the maximum speed of local winds measured at the Isfjord Radio and Svalbard Lufthavn weather stations near the DAS array. The Isfjord Radio station is located at the entrance of the Isfjord and close to the 55 km distance point along the DAS array, whereas Svalbard Lufthavn station is located at the Svalbard Airport in Longyearbyen and close to the start of the DAS array (see Figure 1C). We find no correlation between the local wind speeds and the responses associated with OSGWs. Therefore, we deduce that the OSGW responses visible in the spectrograms are mostly generated from winds or storms outside the Isfjord.

Four linear up-sweep trends of the ocean swells corresponding to distant storms are highlighted in the spectrogram in Figure 9C. Using the procedure described in the Methods section, we can calculate the distance and time taken by an ocean swell to travel from each storm center to the DAS array. Although this procedure has widely been applied to many data sets measured by conventional sensors, we demonstrate it using the ocean-bottom DAS data with detailed calculations for the first time. Table 1 summarizes the calculation of the four storms marked in Figure 9C. By applying geographical and topological constraints (there must be an open seaway between our DAS array and the source of OSGWs), we can retrieve their approximate locations for comparison with public records. The Arctic Ocean is isolated from other oceans by land. The Fram Strait, which lies between Svalbard and Greenland, is the only deep passage into the Arctic Ocean. In addition, the main orientation of our DAS array points toward the Atlantic Ocean. Therefore, the ocean swells detected by our DAS array are produced by storms in the Atlantic Ocean. It is unlikely that our DAS data are dominated by swells caused by storms in the Pacific Ocean through the shallow Bering Strait.

From public records, we can trace all the four linear trends in Figure 9C back to their corresponding storms in the Atlantic Ocean. Storm 1 corresponds to the Tropical Storm Edouard near Bermuda at about 4,100 km away from Longyearbyen, occurring from 2020-07-04 to 2020-07-06 (Pasch, 2021). Storm 2 possibly corresponds to the bomb cyclone in offshore south Brazil at about 13,000 km from Longyearbyen from 2020-06-30 to 2020-07-02 as reported in Gobato and Heidari (2020) and Khalid et al. (2020). According to weather news in Iceland (Ćirić, 2020), Storm 3 should correspond to an extratropical depression between Iceland and Greenland at about

2,400 km away from the DAS array from 2020-07-15 to 2020-07-17. Lastly, Storm 4 probably comes from a storm in a remote region in offshore south Brazil at about 11,000 km from the DAS array on 2020-07-12.

The four storms discussed above are examples of the total 12 storms observed in our data set. Many events like Storm 4 and the stronger trend in the rightmost of the time-frequency spectra in Figure 9C come from remote regions in the South Atlantic Ocean between the eastern coast of South America and the western coast of Africa. As discussed in Landrø et al. (2022), the storms in these remote regions might not affect human and, hence, not be documented. However, they are obviously detected by DAS. Thus, DAS could be a potential storm monitoring system with global coverage.

Future applications

Subsurface exploration

Ocean-bottom DAS can record seismo-acoustic vibrations in broadband frequency ranges. Taweesintananon et al. (2021) use DAS data resulting from marine impulsive seismic sources at a few hundred hertz for subsurface seismic imaging. In addition, Bouffaut et al. (2022) use DAS to record frequency-swept acoustic waves at a few ten hertz produced by whales and generate their corresponding seismic profiles for subsurface exploration. Our data characterization affirms that DAS can record high-quality, low-frequency seismo-acoustic data ranging from 0.01 to 10 Hz, as also shown in other publications (e.g., Sladen et al., 2019; Williams et al., 2019).

In subsurface seismic exploration, the seismo-acoustic waves at the frequencies lower than 10 Hz are usually treated as noise to be removed in data processing. However, the waves in this low-frequency range are interacted with subsurface layers. We clearly see from Figure 3 that the earthquake-related waves give additional data between 0.01 and 10 Hz, in which the S-wave resonances become more pronounced. Previously, we show that the S-wave resonances can be used to determine the structure of the subsurface LVL.

Therefore, it could be possible to further apply DAS to seismic imaging using data with the frequency below 10 Hz. In addition to the higher-frequency data, we could expect more applications of DAS in making use of these low-frequency data for subsurface imaging and exploration. Examples of such applications can be found in Lior et al. (2022) and Spica et al. (2022).

Ocean observation

Functioning marine ecosystems are vital to healthy oceans on which a sustainable future on Earth for all living beings ultimately depends (Danovaro et al., 2020). Marine acoustics plays an important role in studying physical processes in the oceans and their interaction with the solid earth, atmosphere and living organisms. Therefore, passive acoustic monitoring (PAM) is recognized as an important surveillance tool for the Earth's ecosystems, through the studies of ocean ambient sound, marine mammal behavior, glacial/iceberg noise, anthropogenic ocean use, unsanctioned nuclear or other polluting activity, earthquake and tsunami warning, in addition to search and rescue.

We have shown that DAS, as a PAM system, can detect waves from various sources through dynamic interactions between the atmosphere, ocean, and solid earth. It effectively measures ocean-bottom vibrations at low frequency down to 0.01 Hz corresponding to OSGWs. Moreover, it can be used to monitor ocean currents (Williams et al., 2022). Accordingly, sea state can indirectly be monitored by ocean-bottom DAS. Therefore, DAS has many valuable attributes to offer the oceanographic community, nicely complementing existing sensing systems such as satellites (which are broadly limited to very-near-surface observations), buoys, moorings, and floats (which have limited spatial coverage and resolution). The advantages of DAS include broadband and high-resolution spatial and temporal measurement capacities, with data available in real-time to support active marine management and decision-making. Its real-time capability, bringing data from the seafloor, is unmatched by any other system other than fixed installations cabled to shore or supporting long lines to surface buoys, both of which represent expensive and complex engineering challenges. The potential for earthquake and tsunami warning systems alone is therefore remarkable. This sensing network is also possible to create at low cost, because we can use existing submarine telecommunication cables. These cables span more than a million kilometers around all the oceans on the globe, potentially bringing a sensing capability to many less-sampled environments, and perhaps also able to support less developed countries in responsibly managing their maritime resources.

Thus, DAS brings an innovative and game-changing new sensing modality to oceanographic and geophysical observation systems in general. Ocean-bottom DAS can be used to monitor sea state, which is an Essential Climate Variables (ECVs) specified by the Global Climate Observing System (GCOS) (WMO, 2016). Therefore, we believe that DAS can become a valuable new component of the Global Ocean Observing System (GOOS), of the Intergovernmental Oceanographic Commission (IOC) of UNESCO, as discussed in Howe et al. (2019).

CONCLUSION

DAS in an ocean-bottom telecommunication fiber-optic cable can measure various types of ocean-bottom vibrations that are caused by dynamics in the atmosphere, ocean, and solid earth. They comprise (1) the ocean-bottom loading pressure fluctuation corresponding to dynamics in the ocean and atmosphere, and (2) the responses corresponding to seismo-acoustic wave propagation. We clearly describe and compare their characteristics in the ocean-bottom DAS data. Our interpretations are validated by redundant samples from the data that were acquired extensively in spatial and temporal dimensions, over 44 days along 120 km of a submarine fiber-optic cable, extending along the Isfjord in Longyearbyen, Svalbard, across different water depths from 0 to 400 m.

In ocean-bottom DAS data, we observe the signals associated with OSGWs originating from winds and distant storms, together with their reflections at Longyearbyen's shore in shallow water. This observation enables us to trace several responses of ocean swells back to their origins of distant storms in the South Atlantic Ocean up to 13,000 km away from the DAS array in Svalbard. Moreover, we demonstrate a DAS application to near-surface structural mapping using the recorded S-wave resonances. Hence, we may use DAS to delineate the base of LVL which is shallow glacimarine sediments in the Arctic. Therefore, we can expect similar applications to any other LVL of weathered layers in other survey areas. Thanks to its high spatial and temporal resolution, real-time data availability, broadband low-frequency sensitivity and its ability to sense what is happening close to the seafloor, capturing both ocean surface waves and seismo-acoustic events, DAS offers great scientific value to observation systems for the Earth and the Oceans.

ACKNOWLEDGMENTS

The authors acknowledge the Research Council of Norway and the sponsors of the Geophysics and Applied Mathematics in Exploration and Safe production Project (GAMES; grant no. 294404), the Digimon ACT Project (grant no. 299622), and the Centre for Geophysical Forecasting (CGF; grant no. 309960) at NTNU for financial support. The authors thank Alcatel Submarine Networks Norway AS for supporting and operating the OptoDAS interrogator, and Uninett AS for providing access to their fiber-optic cable between Longyearbyen and Ny-Ålesund and operating the data transfer through their network between Svalbard and Trondheim. The authors thank Tim Cato Netland and Daniel Bergh for their technical support on the real-time data transfer. The authors acknowledge Ethan F. Williams and Hefeng Dong for

constructive feedback and discussion on the data characterization.

OPEN RESEARCH

DAS data for this research are available in Taweesintananon and Landrø (2022) via `https://doi.org/10.18710/VPRD2H`. Seismic data from the KBS seismic station in Svalbard used as our reference are available through IRIS web services: `https://service.iris.edu/`. Details on the 2020-07-22 M_{ww} 7.8 earthquake on the Alaska Peninsula are available at USGS website: `https://earthquake.usgs.gov/earthquakes/eventpage/us7000asvb/executive`. The weather data are available through the Norwegian Center for Climate Services (NCCS) at `https://seklima.met.no/observations/`. The tidal data at Longyearbyen (Svalbard) are available through the Norwegian Mapping Authority, Hydrographic Service at `https://www.kartverket.no/en/at-sea/se-havniva`.

AUTHOR CONTRIBUTIONS

M.L., S.E.J., J.K.B., A.H., O.S. and F.S. conceived and designed the experiment. A.H. and F.S. collected data. K.T. processed data and prepared the visualizations. K.T. and M.L. analyzed data with support from J.R.P., S.E.J., R.A.R., L.B. and H.J.K. M.L. and J.R.P. validated research outputs, acquired funding, and managed the project. K.T. wrote the original draft of the manuscript. All the authors conducted review and editing of the manuscript.

COMPETING INTERESTS

Author K.T. is employed by PTT Exploration and Production Public Company Limited. Author J.K.B. is and Author A.H. was employed by Alcatel Submarine Networks Norway AS. Authors O.S. and F.S. are employed by Uninett AS (merged into Sikt in January 2022). The remaining authors declare that the research was conducted in the absence of any commercial or financial relationships that could be construed as a potential conflict of interest.

REFERENCES

Abolfazli, E., J. Liang, Y. Fan, Q. J. Chen, N. D. Walker, and J. Liu, 2020, Surface gravity waves and their role in ocean-atmosphere coupling in the Gulf of Mexico: Journal of Geophysical Research: Oceans, **125**, e2018JC014820.

Airy, G. B., 1841, Tides and waves: Encyclopaedia Metropolitana (1817-1845), **3**, 241–396.

Albaric, J., D. Kühn, M. Ohrnberger, N. Langet, D. Harris, U. Polom, I. Lecomte, and G. Hillers, 2021, Seismic monitoring of permafrost in Svalbard, Arctic Norway: Seismological Research Letters, **92**, 2891–2904.

Angelopoulos, M., P. P. Overduin, F. Miesner, M. N. Grigoriev, and A. A. Vasiliev, 2020, Recent advances in the study of Arctic submarine permafrost: Permafrost and Periglacial Processes, **31**, 442–453.

Ardhuin, F., J. E. Stopa, B. Chapron, F. Collard, R. Husson, R. E. Jensen, J. Johannessen, A. Mouche, M. Passaro, G. D. Quartly, V. Swail, and I. Young, 2019, Observing sea states: Frontiers in Marine Science, **6**, 124.

Barthelemy, X., M. L. Banner, W. L. Peirson, F. Fedele, M. Allis, and F. Dias, 2018, On a unified breaking onset threshold for gravity waves in deep and intermediate depth water: Journal of Fluid Mechanics, **841**, 463–488.

Bigg, G. R., and E. Hanna, 2016, Impacts and effects of ocean warming on the weather, *in* Explaining ocean warming: Causes, scale, effects and consequences: International Union for Conservation of Nature and Natural Resources (IUCN), 359–372.

Bouffaut, L., K. Taweesintananon, H. J. Kriesell, R. Rørstadbotnen, J. R. Potter, M. Landrø, S. E. Johansen, J. K. Brenne, A. Haukanes, O. Schjelderup, and F. Storvik, 2022, Eavesdropping at the speed of light: Distributed acoustic sensing of baleen whales in the Arctic: Frontiers in Marine Science, **9**, 901348.

Bromirski, P. D., and F. K. Duennebier, 2002, The near-coastal microseism spectrum: Spatial and temporal wave climate relationships: Journal of Geophysical Research: Solid Earth, **107**, ESE 5–1–20.

Cavaleri, L., B. Fox-Kemper, and M. Hemer, 2012, Wind waves in the coupled climate system: Bulletin of the American Meteorological Society, **93**, 1651–1661.

Coastal Engineering Research Center, 1984, Shore protection manual, 4 ed.: U.S. Army Engineer Waterways Experiment Station, **1**.

Craik, A. D., 2004, The origins of water wave theory: Annual Review of Fluid Mechanics, **36**, 1–28.

Crawford, W. C., S. C. Webb, and J. A. Hildebrand, 1991, Seafloor compliance observed by long-period pressure and displacement measurements: Journal of Geophysical Research: Solid Earth, **96**, 16151–16160.

Danovaro, R., E. Fanelli, J. Aguzzi, D. Billett, L. Carugati, C. Corinaldesi, A. Dell'Anno, K. Gjerde, A. J. Jamieson, S. Kark, C. McClain, L. Levin, N. Levin, E. Ramirez-Llodra, H. Ruhl, C. R. Smith, P. V. R. Snelgrove, L. Thomsen, C. L. Van Dover, and M. Yasuhara, 2020, Ecological variables for developing a global deep-ocean monitoring and conservation strategy: Nature Ecology & Evolution, **4**, 181–192.

European cooperation in science and technology Action 714, Working Group 3, 2005, Measuring and analysing the directional spectra of ocean waves: EU Publications Office.

Forwick, M., and T. O. Vorren, 2011, Stratigraphy and deglaciation of the Isfjorden area, Spitsbergen: Norwegian Journal of Geology, **90**, 163–179.

Gobato, R., and A. Heidari, 2020, Cyclone Bomb hits Southern Brazil in 2020: Journal of Atmospheric Science Research, **3**, 8–12.

Godin, O. A., and D. M. F. Chapman, 1999, Shear-speed gradients and ocean seismo-acoustic noise resonances: The Journal of the Acoustical Society of America, **106**, 2367–2382.

Godin, O. A., T. J. Deal, and H. Dong, 2021, Physics-based characterization of soft marine sediments using vector sensors: The Journal of the Acoustical Society of America, **149**, 49–61.

Hartog, A. H., 2017, An introduction to distributed optical fibre sensors, 1 ed.: CRC Press.

Howe, B. M., J. Miksis-Olds, E. Rehm, H. Sagen, P. F. Worcester, and G. Haralabus, 2019, Observing the oceans acoustically: Frontiers in Marine Science, **6**, 426.

Jensen, F. B., W. A. Kuperman, M. B. Porter, and H. Schmidt, 2011, Computational ocean acoustics, 2 ed.: Springer New York. Modern Acoustics and Signal Processing.

Kakinuma, T., and Y. Kusuhara, 2022, A 3D numerical study on tsunamis ascending a river: Coastal Engineering Journal, **64**, 272–284.

Khalid, A., A. d. S. de Lima, F. Cassalho, T. Miesse, and C. Ferreira, 2020, Hydrodynamic and wave responses during storm surges on the Southern Brazilian Coast:

A real-time forecast system: Water, **12**, 3397.

Landrø, M., L. Bouffaut, H. J. Kriesell, J. R. Potter, R. A. Rørstadbotnen, K. Taweesintananon, S. E. Johansen, J. K. Brenne, A. Haukanes, O. Schjelderup, and F. Storvik, 2022, Sensing whales, storms, ships and earthquakes using an Arctic fibre optic cable: Scientific Reports, **12**, 19226.

Landrø, M., and P. Hatchell, 2012, Normal modes in seismic data — Revisited: GEOPHYSICS, **77**, W27–W40.

Lin, J., S. Fang, X. Li, R. Wu, and H. Zheng, 2018, Seismological observations of ocean swells Induced by Typhoon Megi using dispersive microseisms recorded in coastal areas: Remote Sensing, **10**, 1437.

Lindsey, N. J., T. C. Dawe, and J. B. Ajo-Franklin, 2019, Illuminating seafloor faults and ocean dynamics with dark fiber distributed acoustic sensing: Science, **366**, 1103–1107.

Lior, I., E. D. Mercerat, D. Rivet, A. Sladen, and J. Ampuero, 2022, Imaging an underwater basin and its resonance modes using optical fiber distributed acoustic sensing: Seismological Research Letters, **93**, 1573–1584.

Lior, I., A. Sladen, D. Mercerat, J.-P. Ampuero, D. Rivet, and S. Sambolian, 2021, Strain to ground motion conversion of distributed acoustic sensing data for earthquake magnitude and stress drop determination: Solid Earth, **12**, 1421–1442.

Mitsuyasu, H., 2002, A historical note on the study of ocean surface waves: Journal of Oceanography, **58**, 109–120.

Munk, W. H., 1950, On the wind-driven ocean circulation: Journal of Atmospheric Sciences, **7**, 80–93.

Munk, W. H., G. R. Miller, F. E. Snodgrass, N. F. Barber, and G. E. R. Deacon, 1963, Directional recording of swell from distant storms: Philosophical Transactions of the Royal Society of London. Series A, Mathematical and Physical Sciences, **255**, 505–584.

Pasch, R. J., 2021, National hurricane center tropical cyclone report: Tropical storm Edouard (AL052020): Technical report, National Oceanic and Atmospheric Administration.

Perlin, M., W. Choi, and Z. Tian, 2013, Breaking waves in deep and intermediate waters: Annual Review of Fluid Mechanics, **45**, 115–145.

Părău, E. I., J.-M. Vanden-Broeck, and M. J. Cooker, 2005, Three-dimensional gravity-capillary solitary waves in water of finite depth and related problems: Physics of Fluids, **17**, 122101.

Rauch, D., 1980, Seismic interface waves in coastal waters: A review: Technical Report SACLANTCEN Report SR-42, North Atlantic Treaty Organization, Italy.

Robein, E., 2010, Velocities, time-imaging and depth-imaging: Principles and methods, 3 ed.: European Association of Geoscientists & Engineers.

Robertson, B., K. Hall, R. Zytner, and I. Nistor, 2013, Breaking waves: Review of characteristic relationships: Coastal Engineering Journal, **55**, 1350002–1–1350002–40.

Schmitt, R. W., 2018, The ocean's role in climate: Oceanography, **31**, 32–40.

Schwardt, M., C. Pilger, P. Gaebler, P. Hupe, and L. Ceranna, 2022, Natural and anthropogenic sources of seismic, hydroacoustic, and infrasonic waves: waveforms and spectral characteristics (and their applicability for sensor calibration): Surveys in Geophysics, **43**, 1265–1361.

Sladen, A., D. Rivet, J. P. Ampuero, L. De Barros, Y. Hello, G. Calbris, and P. Lamare, 2019, Distributed sensing of earthquakes and ocean-solid Earth interactions on seafloor telecom cables: Nature Communications, **10**, 5777.

Spica, Z. J., J. C. Castellanos, L. Viens, K. Nishida, T. Akuhara, M. Shinohara, and T. Yamada, 2022, Subsurface imaging with ocean-bottom distributed acoustic sensing and water phases reverberations: Geophysical Research Letters, **49**, e2021GL095287.

Stephen, R. A., F. N. Spiess, J. A. Collins, J. A. Hildebrand, J. A. Orcutt, K. R. Peal, F. L. Vernon, and F. B. Wooding, 2003, Ocean seismic network pilot experiment: Geochemistry, Geophysics, Geosystems, **4**, 1092.

Stommel, H., 1948, The westward intensification of wind-driven ocean currents: Eos, Transactions American Geophysical Union, **29**, 202–206.

Stull, R., 2017, Practical meteorology: An algebra-based survey of atmospheric science, version 1.02b ed.: University of British Columbia.

Sverdrup, H. U., 1947, Wind-driven currents in a Baroclinic Ocean; with application to the equatorial currents of the Eastern Pacific: Proceedings of the National Academy of Sciences, **33**, 318–326.

Taweesintananon, K., and M. Landrø, 2022, Replication data for DAS4Microseism - Svalbard distributed acoustic sensing (DAS) strain data for oceanographic study.

Taweesintananon, K., M. Landrø, J. K. Brenne, and A. Haukanes, 2021, Distributed acoustic sensing for near-surface imaging using submarine telecommunication cable: A case study in the Trondheimsfjord, Norway: GEOPHYSICS, **86**, B303–B320.

Villas Bôas, A. B., F. Ardhuin, A. Ayet, M. A. Bourassa, P. Brandt, B. Chapron, B. D. Cornuelle, J. T. Farrar, M. R. Fewings, B. Fox-Kemper, S. T. Gille, C. Gommenginger, P. Heimbach, M. C. Hell, Q. Li, M. R. Mazloff, S. T. Merrifield, A. Mouche, M. H. Rio, E. Rodriguez, J. D. Shutler, A. C. Subramanian, E. J. Terrill, M. Tsamados, C. Ubelmann, and E. van Sebille, 2019, Integrated observations of global surface winds, currents, and waves: Requirements and challenges for the next decade: Frontiers in Marine Science, **6**, 425.

Waagaard, O. H., E. Rønnekleiv, A. Haukanes, F. Stabo-Eeg, D. Thingbø, S. Forbord, S. E. Aasen, and J. K. Brenne, 2021, Real-time low noise distributed acoustic sensing in 171 km low loss fiber: OSA Continuum, **4**, 688–701.

Webb, S. C., 1998, Broadband seismology and noise under the ocean: Reviews of Geophysics, **36**, 105–142.

Westwood, E. K., C. T. Tindle, and N. R. Chapman, 1996, A normal mode model for acousto-elastic ocean environments: The Journal of the Acoustical Society of America, **100**, 3631–3645.

Williams, E. F., M. R. Fernández-Ruiz, R. Magalhaes, R. Vanthillo, Z. Zhan, M. González-Herráez, and H. F. Martins, 2019, Distributed sensing of microseisms and teleseisms with submarine dark fibers: Nature Communications, **10**, 5778.

Williams, E. F., Z. Zhan, H. F. Martins, M. R. Fernández-Ruiz, S. Martín-López, M. González-Herráez, and J. Callies, 2022, Surface gravity wave interferometry and ocean current monitoring with ocean-bottom DAS: Journal of Geophysical Research: Oceans, **127**, e2021JC018375.

WMO, 2016, The global observing system for climate: Implementation needs: Technical Report GCOS-200 (GOOS-214), World Meteorological Organization.

Wu, L., Ø. Breivik, and A. Rutgersson, 2019, Ocean-wave-atmosphere interaction processes in a fully coupled modeling system: Journal of Advances in Modeling Earth Systems, **11**, 3852–3874.

Wunsch, C., 2021, The rise of dynamical oceanography—A fragmentary historical note: The Stommel-Munk correspondence, 1947–1953: Oceanography, **34**, 249–253.

Yang, X., and K. Cai, 2022, Limitations of the Yang's breaking wave force formula and its improvement under a wider range of breaker conditions: Open Geosciences, **14**, 1538–1546.

You, Z.-J., 2008, A close approximation of wave dispersion relation for direct calculation of wavelength in any coastal water depth: Applied Ocean Research, **30**, 113–119.

Zhan, Z., M. Cantono, V. Kamalov, A. Mecozzi, R. Müller, S. Yin, and J. C. Castellanos, 2021, Optical polarization–based seismic and water wave sensing on transoceanic cables: Science, **371**, 931–936.

Ćirić, J., 2020, Weather warning for Central Highland, Northwest Iceland.

LIST OF TABLES

1 Estimated origins of the four storms producing ocean swells marked in Figure 9C.

LIST OF FIGURES

1 Maps of the ocean-bottom DAS array. (A) World map showing the array location in Longyearbyen, the epicenter of the 2020-07-22 M_{ww} 7.8 earthquake on the Alaska Peninsula, and the approximate storm locations marked in Figure 9C. (B) Regional map showing the array and the KBS seismic station. (C) Local map showing the array in the Isfjord annotated with the distance in km from the shore in Longyearbyen, and nearby weather stations.

2 DAS strain data from 0 to 15 km along the cable. (A) The strain data in the 1,200-s time window from 2020-07-22T06:00:02Z containing no strong seismic waves from significant earthquakes. (B) The strain data in the 1,200-s time window from 2020-07-22T06:20:02Z containing strong seismic waves (P-, S- and SS-waves) from the 2020-07-22 M_{ww} 7.8 earthquake on the Alaska Peninsula. (C) The water depth profile along the cable.

3 Spectral analysis of DAS strain data. The average power spectra at selected locations along the cable (A) and the power spectral profile (B) in the 1,200-s time window from 2020-07-22T06:00:02Z containing no strong seismic waves from significant earthquakes. The average power spectra at the same locations (C) and the power spectral profile (D) in the 1,200-s time window from 2020-07-22T06:20:02Z containing strong seismic waves (P-, S- and SS-waves) from the 2020-07-22 M_{ww} 7.8 earthquake on the Alaska Peninsula. The average power spectra in (A) and (C) are computed over 251 recording channels (500 m radius) around each location. The numeric annotations highlight the six key events discussed in texts. The colored triangles in (B)

and (D) mark the locations associated with the power spectra in (A) and (C).

4 Band-limited DAS strain data. The strain data from Figure 2A are decomposed by band-pass filters into three frequency bands: (A) 1.2–20 Hz, (B) 0.2–1.2 Hz, and (C) 0.005–0.2 Hz. (D) The water depth profile. The recording time starts from zero at 2020-07-22T06:00:02Z. The colored triangles mark the locations associated with the spectra shown in Figure 3.

5 Frequency analysis of DAS strain data from 0 to 76 km along the cable. (A) The strain data in the 1,200-s time window from 2020-07-22T06:00:02Z containing no strong seismic waves from significant earthquakes. (B) The f-x power spectra. (C) The root-mean-square (RMS) of power (blue) extracted from the frequency range 0.05–0.07 Hz in the f-x power spectra in comparison with the modeled power (red) for OSGWs at 0.06 Hz. (D) The depth profile below SWL of the seafloor and the estimated base of low-velocity layer (LVL).

6 The f-k spectra of DAS strain data. (A–D) The f-k power spectra of the DAS recording from 2020-07-22T06:00:02Z (Figures 2A and 5A) at 34.03, 11.56, 4.20 and 1.75 km along the cable from shore, each of which is computed from the 1,200-s time window over its surrounding 1,001 recording channels (2 km radius). (E–H) The f-k power spectra of the DAS recording from 2020-07-22T06:20:02Z (Figures 2B and 8A) at the same positions and the same window sizes as for A–D. The wavenumber, $k/(2\pi)$, is referencing the cable distance from the shore in Longyearbyen: $k > 0$ for waves propagating to the West (the North Atlantic Ocean), and $k < 0$ for waves propagating to the East (the inner part of the Isfjord).

7 Spectrograms (t-f spectra) of DAS strain data. Spectrograms at (A) 1.75,

(B) 4.20 and (C) 11.56 km along the cable from shore. (D) Sea level in Longyearbyen (Svalbard) with respect to the average sea level during the experiment. (E) Maximum wind speeds measured at Isfjord Radio and Svalbard Lufthavn weather stations (see Figure 1C). All the spectrograms are computed from the average power spectrum over 251 recording channels (500 m radius) around the selected locations within a 300-s time window on an hourly basis. White vertical stripes in the spectrograms indicate dropout periods in the real-time data transfer.

8 Frequency analysis of DAS strain data from 0 to 76 km along the cable. (A) The strain data in the 1,200-s time window from 2020-07-22T06:20:02Z containing strong seismic waves (P-, S- and SS-waves) from the 2020-07-22 M_{ww} 7.8 earthquake on the Alaska Peninsula. (B) The f-x power spectra. (C) The RMS power extracted along the first S-wave resonance frequency ($f_{s,1}$) picks in the f-x power spectra. (D) The depth profile below SWL of the seafloor and the estimated base of LVL.

9 Spectrograms for storm monitoring. The same spectrograms as Figure 7, but with linear scale for the vertical axes, (A) 1.75, (B) 4.20 and (C) 11.56 km along the cable from shore. (D) Sea level in Longyearbyen (Svalbard) with respect to the average sea level during the experiment. (E) Maximum wind speeds measured at Isfjord Radio and Svalbard Lufthavn weather stations (see Figure 1C). Four storm events marked in (C) are discussed in texts. All the spectrograms are computed from the average power spectrum over 251 recording channels (500 m radius) around the selected locations within a 300-s time window on an hourly basis.

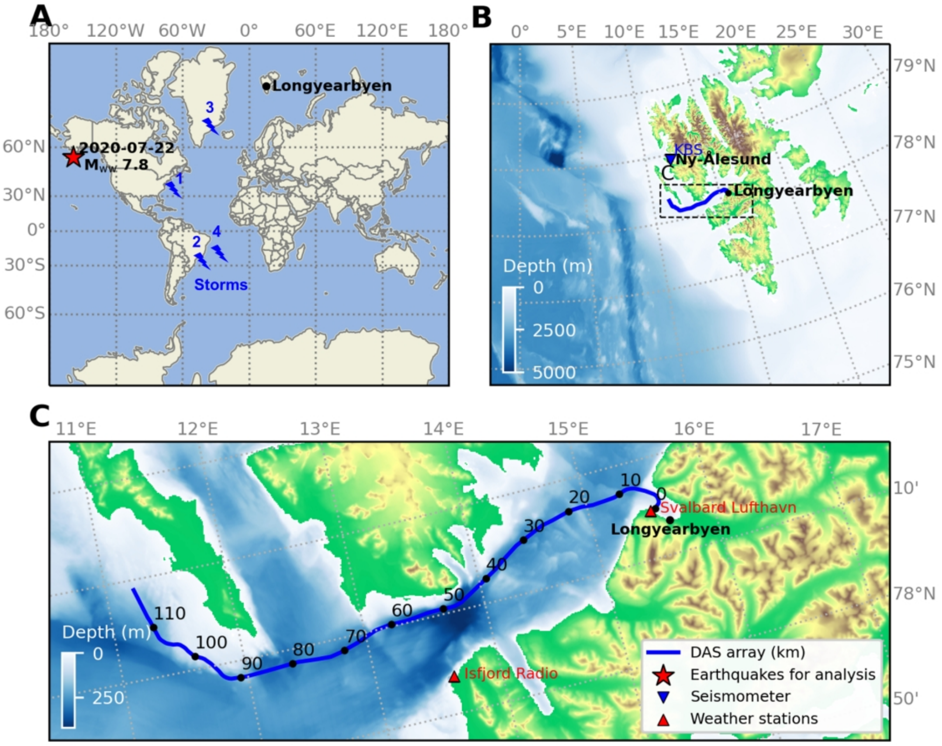

Figure 1: Maps of the ocean-bottom DAS array. (A) World map showing the array location in Longyearbyen, the epicenter of the 2020-07-22 M_{ww} 7.8 earthquake on the Alaska Peninsula, and the approximate storm locations marked in Figure 9C. (B) Regional map showing the array and the KBS seismic station. (C) Local map showing the array in the Isfjord annotated with the distance in km from the shore in Longyearbyen, and nearby weather stations.

450x337mm (118 x 118 DPI)

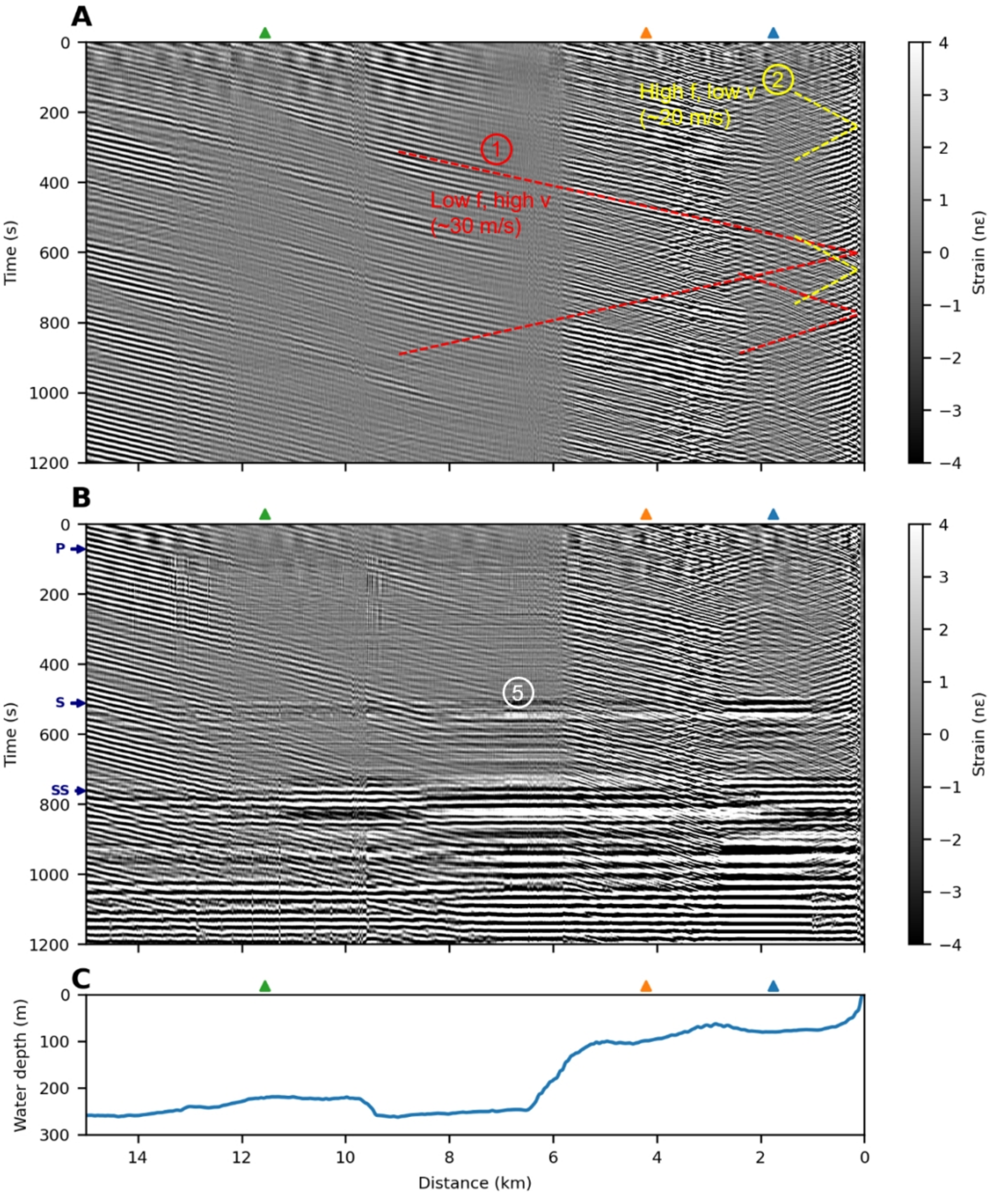

Figure 2: DAS strain data from 0 to 15 km along the cable. (A) The strain data in the 1,200-s time window from 2020-07-22T06:00:02Z containing no strong seismic waves from significant earthquakes. (B) The strain data in the 1,200-s time window from 2020-07-22T06:20:02Z containing strong seismic waves (P-, S- and SS-waves) from the 2020-07-22 M_{ww} 7.8 earthquake on the Alaska Peninsula. (C) The water depth profile along the cable.

250x300mm (130 x 130 DPI)

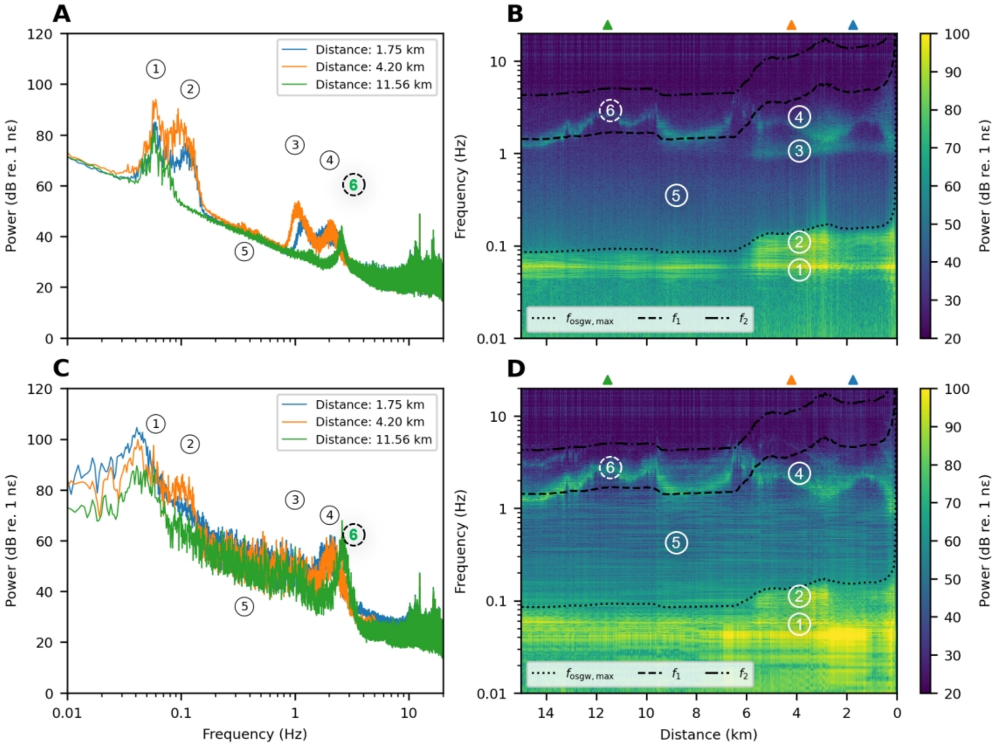

Figure 3: Spectral analysis of DAS strain data. The average power spectra at selected locations along the cable (A) and the power spectral profile (B) in the 1,200-s time window from 2020-07-22T06:00:02Z containing no strong seismic waves from significant earthquakes. The average power spectra at the same locations (C) and the power spectral profile (D) in the 1,200-s time window from 2020-07-22T06:20:02Z containing strong seismic waves (P-, S- and SS-waves) from the 2020-07-22 M_{ww} 7.8 earthquake on the Alaska Peninsula. The average power spectra in (A) and (C) are computed over 251 recording channels (500 m radius) around each location. The numeric annotations highlight the six key events discussed in texts. The colored triangles in (B) and (D) mark the locations associated with the power spectra in (A) and (C).

343x257mm (130 x 130 DPI)

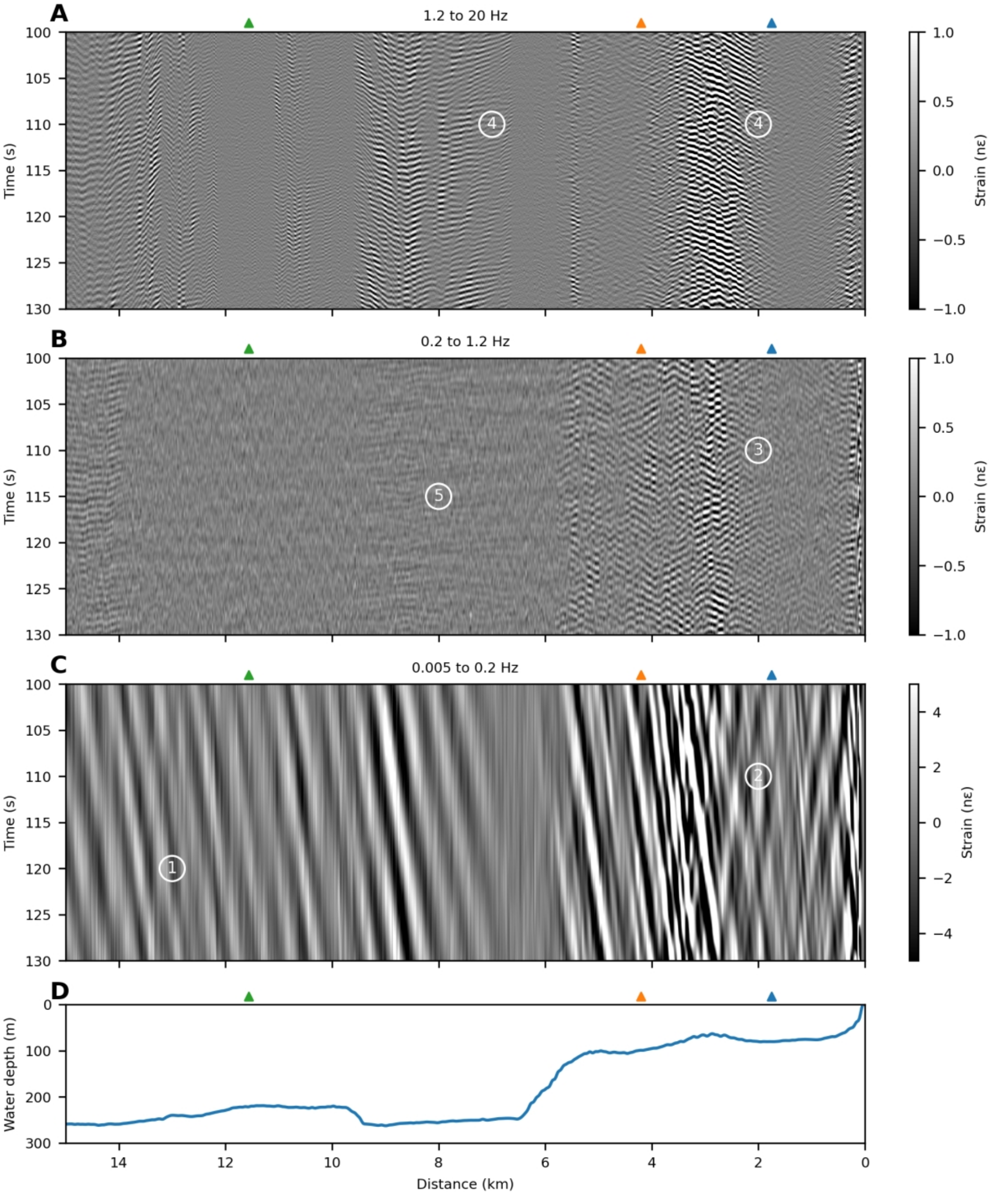

Figure 4: Band-limited DAS strain data. The strain data from Figure 2A are decomposed by band-pass filters into three frequency bands: (A) 1.2–20 Hz, (B) 0.2–1.2 Hz, and (C) 0.005–0.2 Hz. (D) The water depth profile. The recording time starts from zero at 2020-07-22T06:00:02Z. The colored triangles mark the locations associated with the spectra shown in Figure 3.

450x540mm (118 x 118 DPI)

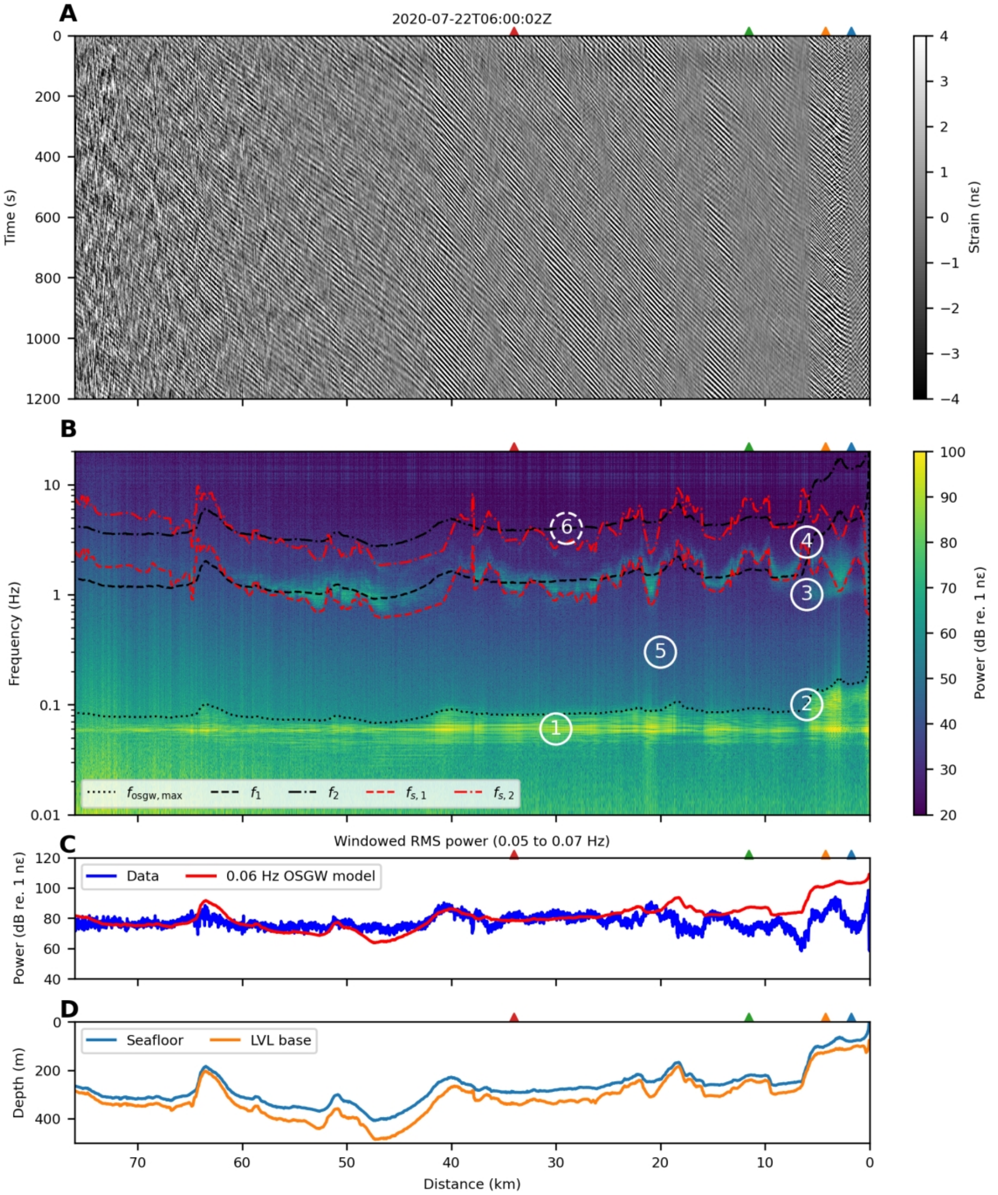

Figure 5: Frequency analysis of DAS strain data from 0 to 76 km along the cable. (A) The strain data in the 1,200-s time window from 2020-07-22T06:00:02Z containing no strong seismic waves from significant earthquakes. (B) The *f-x* power spectra. (C) The root-mean-square (RMS) of power (blue) extracted from the frequency range 0.05–0.07 Hz in the *f-x* power spectra in comparison with the modeled power (red) for OSGWs at 0.06 Hz. (D) The depth profile below SWL of the seafloor and the estimated base of low-velocity layer (LVL).

450x540mm (118 x 118 DPI)

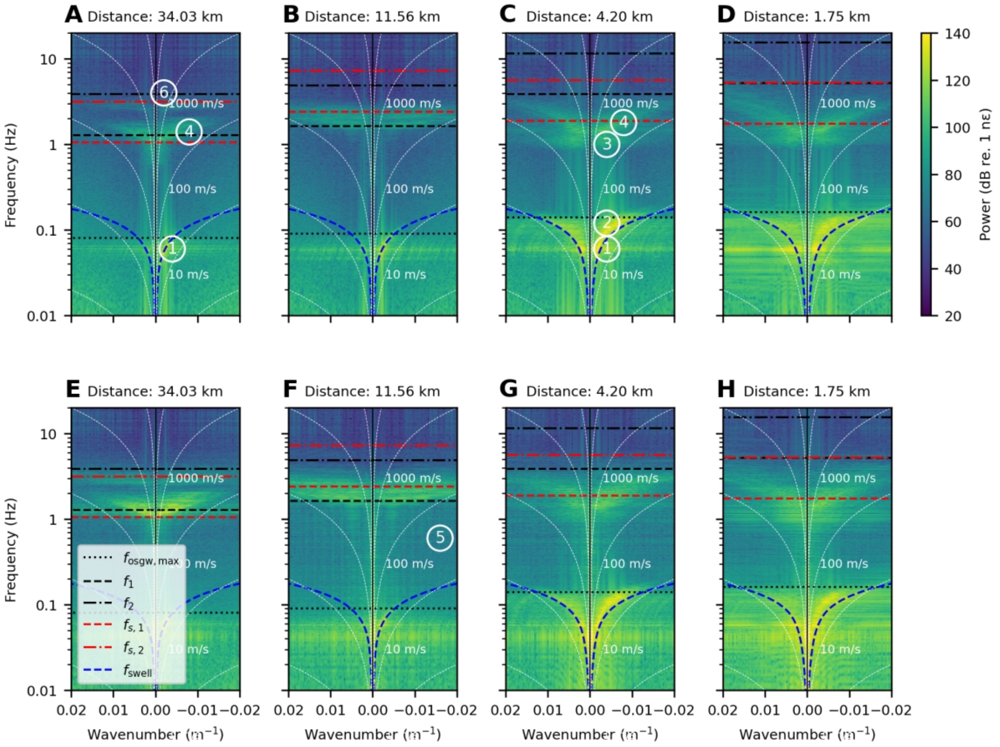

Figure 6: The *f*-*k* spectra of DAS strain data. (A–D) The *f*-*k* power spectra of the DAS recording from 2020-07-22T06:00:02Z (Figures 2A and 5A) at 34.03, 11.56, 4.20 and 1.75 km along the cable from shore, each of which is computed from the 1,200-s time window over its surrounding 1,001 recording channels (2 km radius). (E–H) The *f*-*k* power spectra of the DAS recording from 2020-07-22T06:20:02Z (Figures 2B and 8A) at the same positions and the same window sizes as for A–D. The wavenumber, *k* / (2*π*), is referencing the cable distance from the shore in Longyearbyen: *k* > 0 for waves propagating to the West (the North Atlantic Ocean), and *k* < 0 for waves propagating to the East (the inner part of the Isfjord).

450x337mm (118 x 118 DPI)

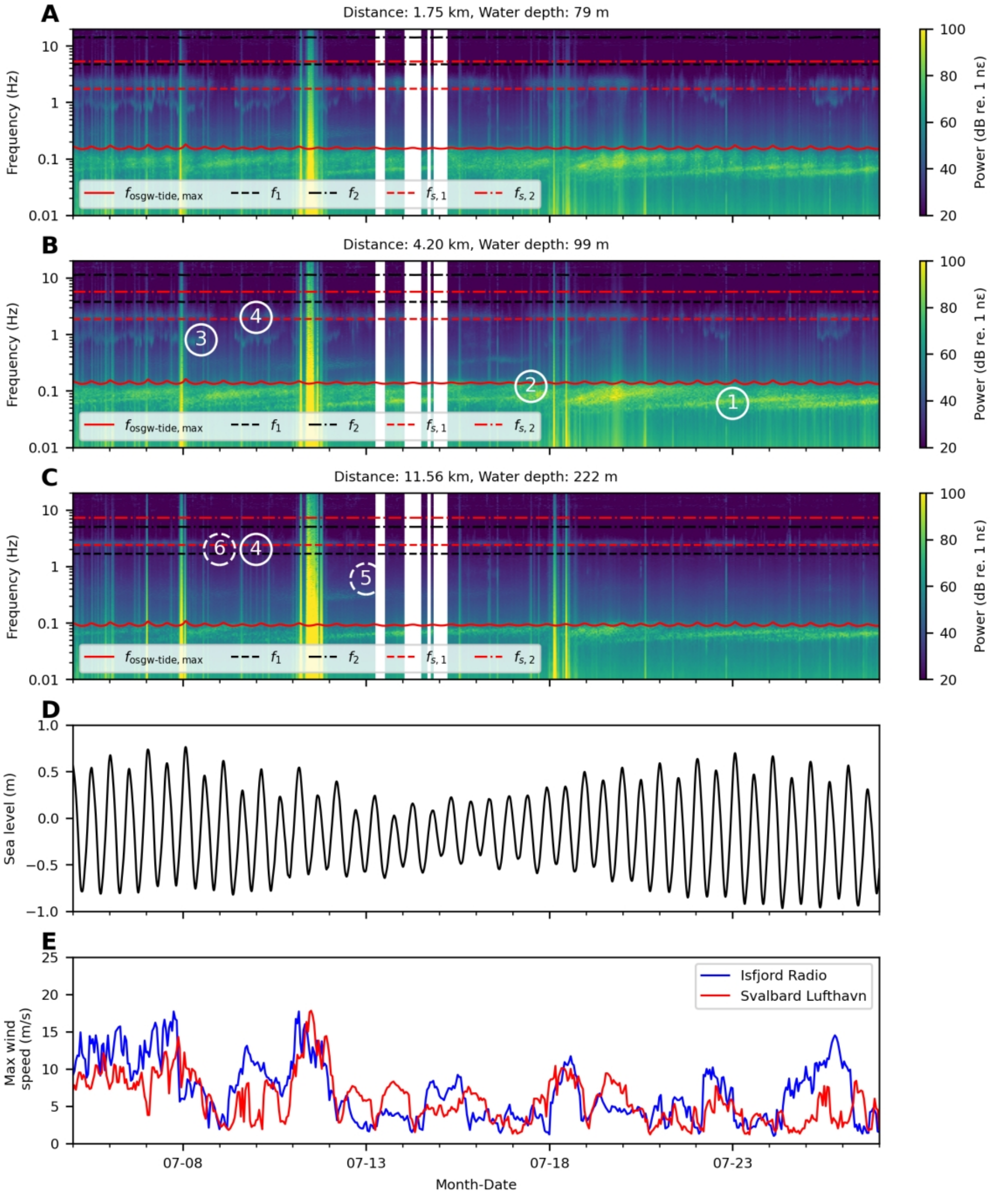

Figure 7: Spectrograms (t-f spectra) of DAS strain data. Spectrograms at (A) 1.75, (B) 4.20 and (C) 11.56 km along the cable from shore. (D) Sea level in Longyearbyen (Svalbard) with respect to the average sea level during the experiment. (E) Maximum wind speeds measured at Isfjord Radio and Svalbard Lufthavn weather stations (see Figure 1C). All the spectrograms are computed from the average power spectrum over 251 recording channels (500 m radius) around the selected locations within a 300-s time window on an hourly basis. White vertical stripes in the spectrograms indicate dropout periods in the real-time data transfer.

450x540mm (118 x 118 DPI)

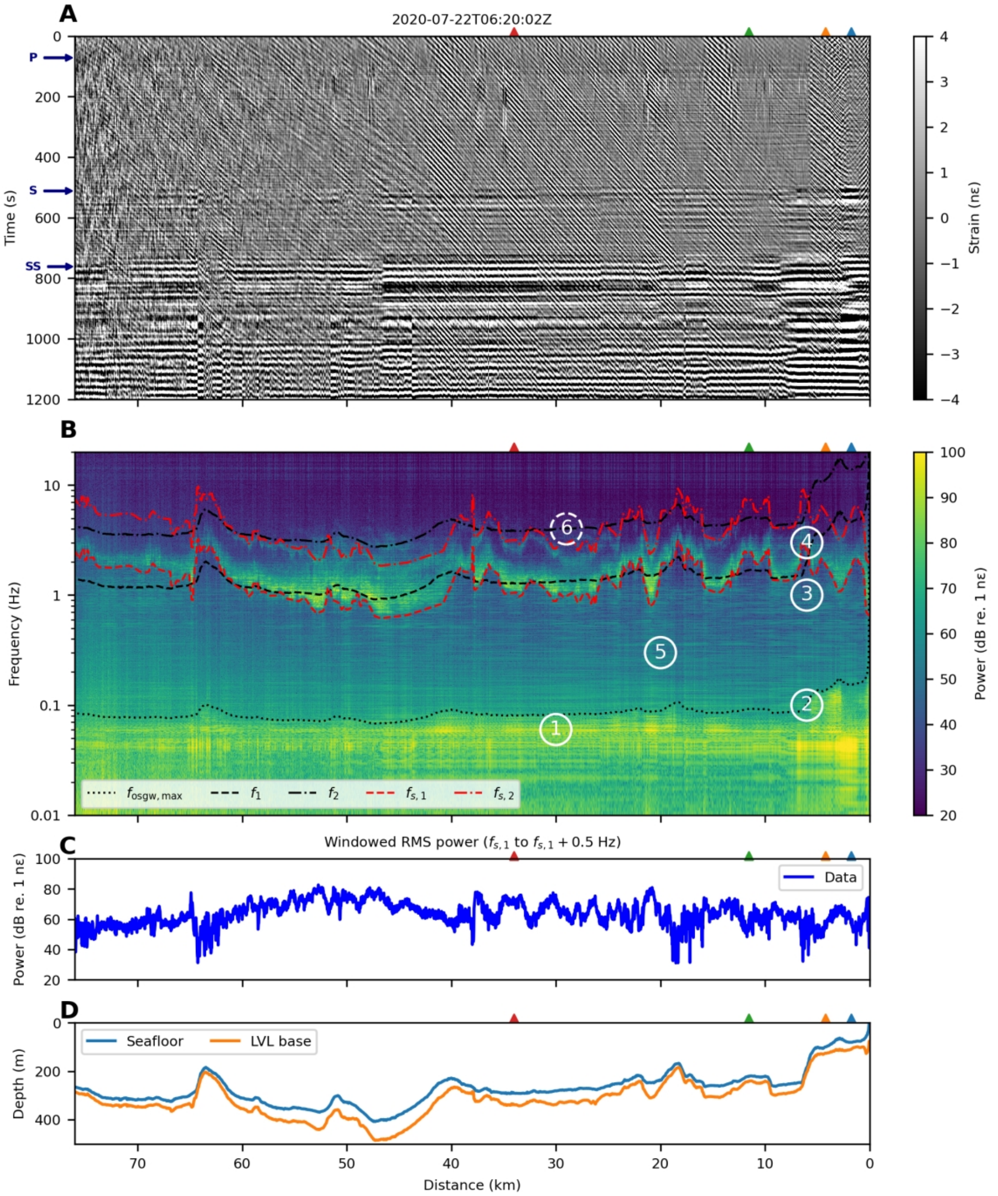

Figure 8: Frequency analysis of DAS strain data from 0 to 76 km along the cable. (A) The strain data in the 1,200-s time window from 2020-07-22T06:20:02Z containing strong seismic waves (P-, S- and SS-waves) from the 2020-07-22 M_{ww} 7.8 earthquake on the Alaska Peninsula. (B) The *f-x* power spectra. (C) The RMS power extracted along the first S-wave resonance frequency ($f_{s,1}$) picks in the *f-x* power spectra. (D) The depth profile below SWL of the seafloor and the estimated base of LVL.

450x540mm (118 x 118 DPI)

DOI:10.1190/geo2022-0435.1

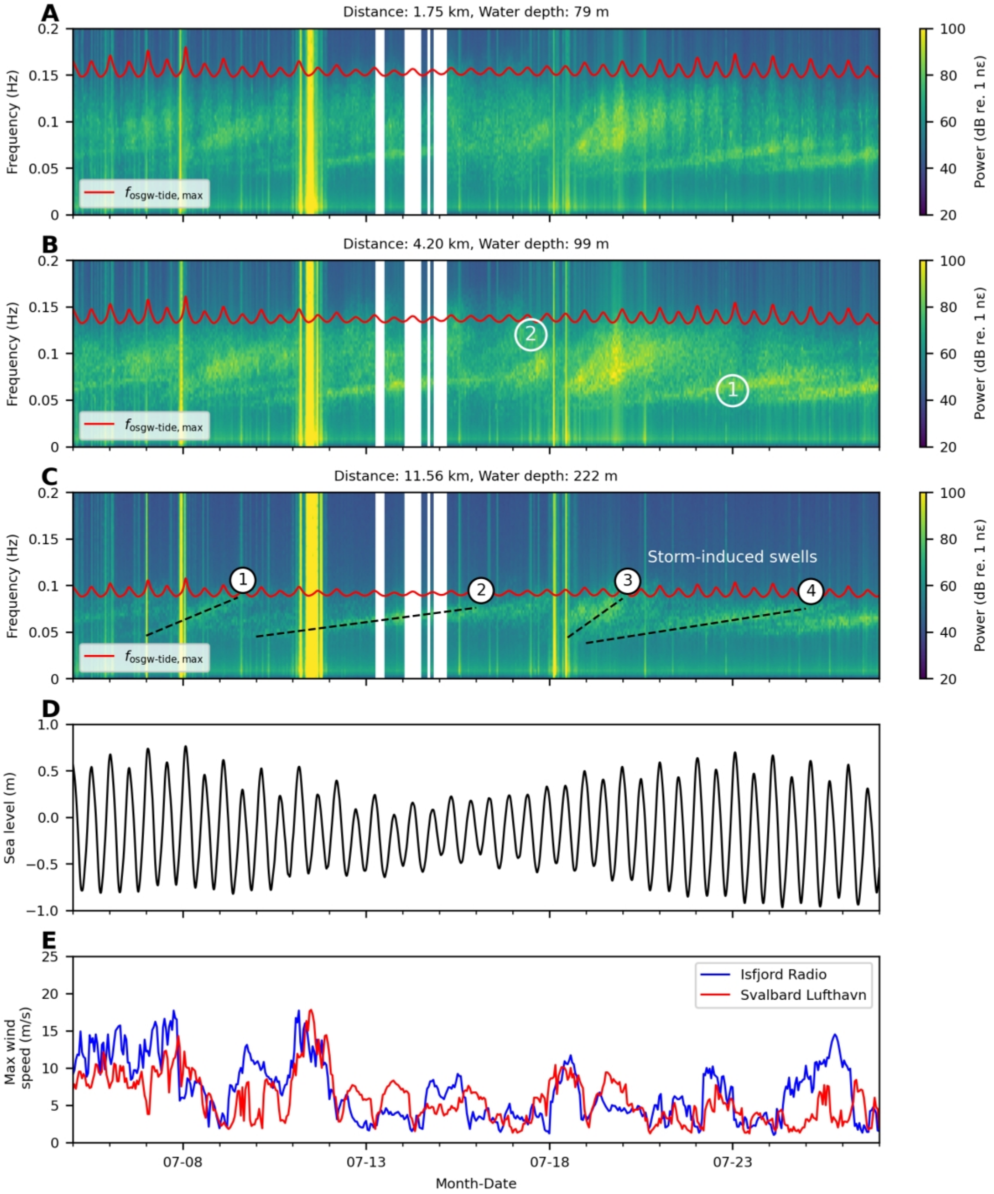

Figure 9: Spectrograms for storm monitoring. The same spectrograms as Figure 7, but with linear scale for the vertical axes, (A) 1.75, (B) 4.20 and (C) 11.56 km along the cable from shore. (D) Sea level in Longyearbyen (Svalbard) with respect to the average sea level during the experiment. (E) Maximum wind speeds measured at Isfjord Radio and Svalbard Lufthavn weather stations (see Figure 1C). Four storm events marked in (C) are discussed in texts. All the spectrograms are computed from the average power spectrum over 251 recording channels (500 m radius) around the selected locations within a 300-s time window on an hourly basis.

450x540mm (118 x 118 DPI)

Parameters	**Storm 1**	**Storm 2**	**Storm 3**	**Storm 4**
Start time at DAS (t_0)	2020-07-07 T00:00:00Z	2020-07-10 T00:00:00Z	2020-07-18 T12:00:00Z	2020-07-19 T00:00:00Z
End time at DAS (t_1)	2020-07-09 T12:00:00Z	2020-07-16 T00:00:00Z	2020-07-20 T00:00:00Z	2020-07-25 T00:00:00Z
Frequency at start time (f_0)	0.046 Hz	0.045 Hz	0.044 Hz	0.038 Hz
Frequency at end time (f_1)	0.087 Hz	0.076 Hz	0.086 Hz	0.075 Hz
Travel distance (x in equation 14)	4,113 km	13,055 km	2,409 km	10,938 km
Group velocity for the lowest-frequency swell (c_g in equation 15 with $f = f_0$)	16.97 m/s	17.35 m/s	17.74 m/s	20.54 m/s
Traveltime for the lowest-frequency swell (t in equation 16)	67.32 hours	209.03 hours	37.71 hours	147.89 hours
Estimated time at source ($t_0 - t$)	2020-07-04 T04:40:00Z	2020-07-01 T06:58:00Z	2020-07-16 T22:17:00Z	2020-07-12 T20:06:00Z

Table 1: Estimated origins of the four storms producing ocean swells marked in Figure 9C.

DATA AND MATERIALS AVAILABILITY

Data associated with this research are available and can be accessed via the following URL:lt;brgt; Note: A digital object identifier (DOI) linking to the data in a general or discipline-specific data repository is strongly preferred.

DOI:10.1190/geo2022-0435.1